

# SALAD-Pan: Sensor-Agnostic Latent Adaptive Diffusion for Pan-Sharpening

Junjie Li<sup>1</sup> Congyang Ou<sup>1</sup> Haokui Zhang<sup>\*1</sup> Guoting Wei<sup>1</sup> Shengqin Jiang<sup>2</sup> Ying Li<sup>1</sup> Chunhua Shen<sup>3</sup>

## Abstract

Recently, diffusion models bring novel insights for Pan-sharpening and notably boost fusion precision. However, most existing models perform diffusion in the pixel space and train distinct models for different multispectral (MS) imagery, suffering from high latency and sensor-specific limitations. In this paper, we present SALAD-Pan, a sensor-agnostic latent space diffusion method for efficient pansharpening. Specifically, SALAD-Pan trains a band-wise single-channel VAE to encode high-resolution multispectral (HRMS) into compact latent representations, supporting MS images with various channel counts and establishing a basis for acceleration. Then spectral physical properties, along with PAN and MS images, are injected into the diffusion backbone through unidirectional and bidirectional interactive control structures respectively, achieving high-precision fusion in the diffusion process. Finally, a lightweight cross-spectral attention module is added to the central layer of diffusion model, reinforcing spectral connections to boost spectral consistency and further elevate fusion precision. Experimental results on GaoFen-2, QuickBird, and WorldView-3 demonstrate that SALAD-Pan outperforms state-of-the-art diffusion-based methods across all three datasets, attains a 2–3 $\times$  inference speedup, and exhibits robust zero-shot (cross-sensor) capability. Code will be released at <https://github.com/JJLibra/SALAD-Pan>.

## 1. Introduction

Existing earth observation systems face a fundamental trade-off between spatial and spectral resolution due to physical

<sup>1</sup>School of Cyberspace Security, Northwestern Polytechnical University, Xi'an, Shanxi, China <sup>2</sup>School of Computer Science, Nanjing University of Information Science and Technology, Nanjing, Jiangsu, China <sup>3</sup>Zhejiang University, Hangzhou, Zhejiang, China. Correspondence to: Haokui Zhang <hkzhang@nwpu.edu.cn>.

sensor limitations (Zhang et al., 2023). These systems can only capture either low-resolution multispectral (LRMS) images with rich spectral information or high-resolution panchromatic (PAN) images with a single band. Pansharpening addresses this limitation by fusing LRMS and PAN images to generate high-resolution multispectral (HRMS) imagery that possesses both high spatial resolution and rich spectral information, which is critical for land cover mapping (Dong et al., 2023), change detection (Wang & Wu, 2025), and disaster assessment (Kalluri et al., 2024).

Traditional pansharpening methods typically include component substitution (CS) methods (Vivone et al., 2014), multi-resolution analysis (MRA) methods (Nunez et al., 2002), and variational optimization (VO) techniques (Duran et al., 2017). These approaches employ hand-crafted transformations, multi-scale decompositions, or optimization models. However, they struggle to optimally balance spatial enhancement and spectral preservation, often yielding suboptimal results (Javan et al., 2021). In recent years, deep learning methods have gained prominence by learning complex nonlinear mappings directly from data. Convolutional neural networks (CNNs) and Transformer-based pansharpening methods, leveraging their strong local and global modeling capabilities, have achieved superior performance over traditional methods (Vivone et al., 2024). Despite this progress, effectively capturing the complex cross-modal joint distribution between PAN and MS modalities to generate high-quality HRMS with both rich spectral and spatial information remains a fundamental challenge.

Diffusion models have recently emerged as a promising alternative for pansharpening (Cao et al., 2024; 2025). By modeling complex distributions through iterative denoising processes, they can effectively learn cross-modal relationships between PAN and MS modalities (Kawar et al., 2022). PanDiff (Meng et al., 2023) first introduces denoising diffusion probabilistic models (DDPM) (Ho et al., 2020) to pansharpening, where PAN and LRMS images serve as conditional inputs to guide the denoising process, rather than being directly fused as in aforementioned methods. Subsequent works have further advanced this paradigm by refining the conditioning mechanisms, such as introducing spatial-spectral decomposition (Zhong et al., 2024) to separately model spatial and spectral features, and employing semantic-guided routing (Xing et al., 2025) to enhance cross-sensor

generalization. Despite these advances, existing diffusion-based pansharpening methods still face two critical limitations: 1) they typically perform diffusion directly at the pixel level, resulting in substantial computational overhead and high inference latency; 2) they are often sensor-specific, requiring distinct models to be trained for different satellite sensors due to variations in spectral band configurations across sensors.

To address these challenges, we propose **SALAD-Pan**, a sensor-agnostic latent space diffusion framework for efficient pansharpening. SALAD-Pan employs a two-stage training strategy. In Stage I, we train a band-wise single-channel VAE to encode each spectral band of HRMS independently into a compact latent representation. This band-wise encoding strategy enables handling arbitrary spectral bands across different sensors, establishing a solid foundation for both computational efficiency and cross-sensor generalization. In Stage II, we perform conditional latent diffusion with disentangled spatial-spectral conditioning. HRMS is first encoded band-by-band into latent features using the pretrained VAE encoder. We then inject multi-modal conditioning through carefully designed control structures: PAN provides spatial guidance, LRMS provides spectral information, and frozen CLIP (Radford et al., 2021) text embeddings provide sensor-aware physical metadata, enabling a single unified model to adapt to different sensors without retraining. Notably, we design bidirectional interactions between both conditioning branches (spatial and spectral) and the diffusion backbone, allowing adaptive feature refinement throughout the denoising process. This disentangled yet interactive strategy effectively captures the cross-modal joint distribution between PAN and MS modalities, enabling high-precision fusion in the compact latent space. Furthermore, to address the potential band independence introduced by the band-wise VAE processing, we introduce a lightweight Region-based Cross-Band Attention (RCBA) module that captures dependencies across spectral bands, thereby enhancing spectral consistency and further improving fusion quality. Our main contributions are:

- We propose SALAD-Pan, a sensor-agnostic latent space diffusion framework for pansharpening. A band-wise single-channel VAE is trained to convert arbitrary spectral bands to a unified latent space for acceleration. To the best of our knowledge, this is the first cross-sensor applicable latent space constructed and applied to the pansharpening task.
- A bidirectional interaction design is proposed to guide the diffusion process, where PAN, LRMS, and sensor-specific prompts are jointly injected. More fine-grained interactions better coordinate the conditioning signals, and iterative feature refinement further improves performance. Additionally, a lightweight RCBA module

is introduced to enhance inter-band consistency and fusion precision.

- Extensive experiments demonstrate that SALAD-Pan outperforms previous methods across three benchmarks, achieves  $2\text{--}3\times$  inference speedup, and exhibits strong zero-shot cross-sensor generalization.

## 2. Related Work

**Traditional Methods** are generally grouped into component substitution (CS), multi-resolution analysis (MRA), and variational optimization (VO) families (Javan et al., 2021). CS methods transform MS into alternative color spaces (e.g., IHS, PCA, GS), replace spatial components with PAN information, and transform back, offering computational efficiency but often suffering from spectral distortion (Vivone et al., 2014). MRA methods inject spatial details extracted from PAN into upsampled MS through multi-scale decompositions such as wavelets or Laplacian pyramids, better preserving spectral fidelity but prone to spatial artifacts (Nunez et al., 2002). VO methods solve pansharpening via regularized energy minimization, with theoretical guarantees but high complexity and sensitive hyperparameters (Duran et al., 2017).

**Deep Learning Approaches** have become dominant in pansharpening by learning complex nonlinear mappings from data (Deng et al., 2022; Ciotola et al., 2022; Huang et al., 2025a). CNN-based approaches such as PNN (Masi et al., 2016) and PanNet (Yang et al., 2017) employ multi-scale convolutional architectures to extract local spatial-spectral features from concatenated PAN and MS inputs. Transformer-based methods such as PanFormer (Zhou et al., 2022) and PanAdapter (Wu et al., 2025) improve fusion via long-range self-attention, but remain sensor-specific, limiting cross-sensor generalization. More fundamentally, both CNN and Transformer approaches adopt deterministic regression frameworks that directly predict HRMS outputs without explicitly modeling the probabilistic distribution of the cross-modal relationship between PAN and MS modalities (Kawar et al., 2022).

**Diffusion Models** have emerged as a powerful paradigm for pansharpening, explicitly capturing the PAN-MS cross-modal distribution via iterative denoising (Xing et al., 2024b;a; Zhang et al., 2025; Kim et al., 2025). PanDiff (Meng et al., 2023) pioneers DDPM-based pansharpening by jointly conditioning on coupled PAN and LRMS inputs. SSDiff (Zhong et al., 2024) refines conditioning through spatial-spectral decomposition to separately model spatial and spectral features, while SGDiff (Xing et al., 2025) employs semantic-guided routing to improve feature alignment. However, these methods still suffer from two key limitations: (i) iterative denoising in pixel space is

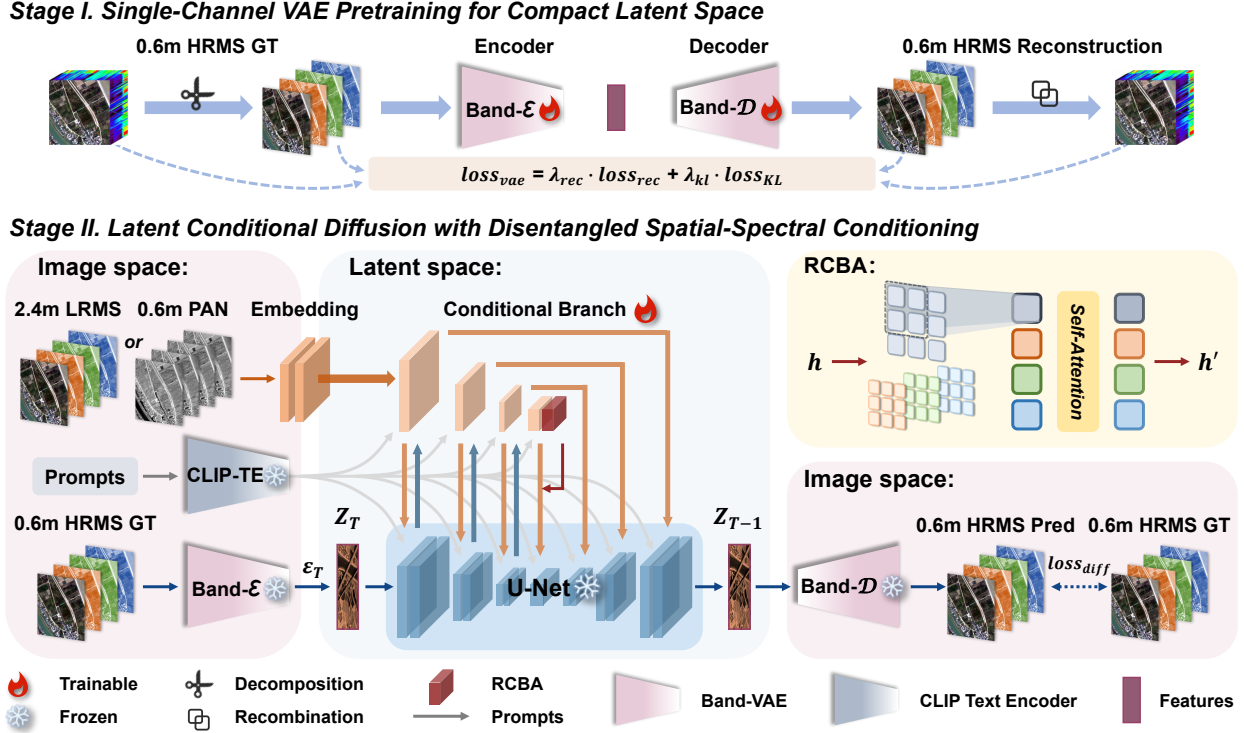


**Figure 1. Overview of SALAD-Pan.** **Stage I** trains a band-wise single-channel VAE to map each HRMS band into a compact latent space. **Stage II** performs band-wise conditional latent diffusion with disentangled spatial-spectral conditioning: a spatial branch encodes PAN for spatial guidance, while a spectral branch encodes the upsampled LRMS band-by-band for spectral guidance. We use hybrid coupling: bidirectional interaction in the encoder and unidirectional (branch→backbone) control in the mid block and decoder. RCBA improves inter-band consistency, and sensor-aware metadata prompts from a frozen CLIP text encoder provide additional conditioning.

computationally expensive since each step operates at full resolution; and (ii) fixed-dimensional band encodings hinder cross-sensor transfer, requiring retraining when band configurations change.

### 3. Methodology

#### 3.1. Problem Formulation

Pansharpening fuses a low-resolution multispectral (LRMS) image  $\mathbf{M} \in \mathbb{R}^{B \times h \times w}$  and a high-resolution panchromatic (PAN) image  $\mathbf{P} \in \mathbb{R}^{1 \times H \times W}$  to generate a high-resolution multispectral (HRMS) image  $\mathbf{X} \in \mathbb{R}^{B \times H \times W}$ , where  $B$  denotes the number of spectral bands and the spatial scale ratio is  $r = H/h = W/w$ . The objective is to reconstruct  $\mathbf{X}$  that preserves the spectral characteristics of  $\mathbf{M}$  while capturing the spatial details from  $\mathbf{P}$ .

Existing diffusion-based pansharpening methods perform denoising directly in pixel space on full-resolution HRMS images throughout the diffusion chain, resulting in high computational cost and slow inference. In contrast, SALAD-Pan performs diffusion in a compact latent space with band-wise processing, where each band  $\mathbf{X}^{(b)} \in \mathbb{R}^{1 \times H \times W}$  ( $b = 1, \dots, B$ ) is encoded and processed independently,

substantially reducing computational overhead.

#### 3.2. Framework Overview

As illustrated in Figure 1, SALAD-Pan employs a two-stage training strategy. **Stage I: Single-Channel VAE Pretraining.** We train a band-wise single-channel VAE that encodes each spectral band of HRMS independently into compact latent representations. This band-wise processing strategy naturally supports arbitrary numbers of spectral bands, enabling cross-sensor generalization. **Stage II: Latent Conditional Diffusion.** With the VAE encoder frozen, we perform conditional diffusion in the latent space. The diffusion backbone receives disentangled spatial-spectral conditioning from PAN and LRMS images via dual control branches, along with sensor-aware physical metadata via text cross-attention. A lightweight region-based cross-band attention (RCBA) module at the central layer further enhances spectral consistency.

#### 3.3. Band-wise Single-channel VAE

In Stage I, we train a VAE to enable diffusion in a compact latent space, which significantly reduces computational cost compared to pixel-space diffusion. However, existing

VAEs (e.g., SD-VAE (Rombach et al., 2022)) are typically designed for three-channel RGB images, creating an application gap for HRMS images with varying numbers of spectral bands across different sensors. To bridge this gap, we propose a band-wise single-channel VAE that processes each spectral band independently through a shared encoder-decoder architecture. This design naturally supports arbitrary band configurations across sensors and avoids inter-band interference, enabling precise encoding of each band’s spectral characteristics.

Specifically, we modify the first and last convolutional layers that interface with the image channels to operate on single-channel inputs. The VAE first encodes each band of HRMS  $\mathbf{X}^{(b)} \in \mathbb{R}^{1 \times H \times W}$  and produces a diagonal Gaussian posterior  $q_\phi(\mathbf{z} \mid \mathbf{X}^{(b)}) = \mathcal{N}(\boldsymbol{\mu}_\phi(\mathbf{X}^{(b)}), \text{diag}(\boldsymbol{\sigma}_\phi^2(\mathbf{X}^{(b)})))$ , from which a latent representation  $\mathbf{z} \in \mathbb{R}^{C \times h' \times w'}$  is sampled, where  $h' \ll H$  and  $w' \ll W$ . Subsequently, the decoder reconstructs the band from  $\mathbf{z}$  as  $\hat{\mathbf{X}}^{(b)} = \mathcal{D}_\psi(\mathbf{z})$ .

After VAE pretraining, we use the mean of the posterior distribution as the deterministic latent representation and apply a fixed scaling factor  $\kappa_{\text{vae}}$  to normalize the latent magnitude for the subsequent diffusion process:

$$\mathbf{z}_0^{(b)} = \kappa_{\text{vae}} \cdot \boldsymbol{\mu}_\phi(\mathbf{X}^{(b)}), \quad \hat{\mathbf{X}}^{(b)} = \mathcal{D}_\psi\left(\mathbf{z}_0^{(b)} / \kappa_{\text{vae}}\right), \quad (1)$$

where  $\kappa_{\text{vae}}$  is estimated from empirical latent statistics and remains fixed thereafter.

### 3.4. Latent Conditional Diffusion Model

In Stage II, we train a conditional diffusion model to generate the clean latent  $\mathbf{z}^{(b)}$  for each band  $b$ , with the pretrained VAE frozen. The generation is conditioned on three types of information: (i) the PAN image providing high-frequency spatial details, (ii) the upsampled LRMS band offering radiometric guidance, and (iii) sensor-aware metadata encoded as text prompts for contextual information.

**Latent diffusion formulation.** For each band  $b$ , we apply a standard DDPM (Ho et al., 2020) forward process in the latent space:

$$\mathbf{z}_t^{(b)} = \sqrt{\bar{\alpha}_t} \mathbf{z}_0^{(b)} + \sqrt{1 - \bar{\alpha}_t} \boldsymbol{\epsilon}^{(b)}, \quad \boldsymbol{\epsilon}^{(b)} \sim \mathcal{N}(\mathbf{0}, \mathbf{I}), \quad (2)$$

where  $\bar{\alpha}_t = \prod_{i=1}^t \alpha_i$  and  $t \in \{1, \dots, T\}$ . The denoiser predicts the added noise:

$$\hat{\boldsymbol{\epsilon}}^{(b)} = f_\theta\left(\mathbf{z}_t^{(b)}, t; \mathbf{P}, \tilde{\mathbf{M}}^{(b)}, \mathcal{E}(s_{S,b})\right), \quad (3)$$

where  $\tilde{\mathbf{M}} = \text{Up}(\mathbf{M}) \in \mathbb{R}^{B \times H \times W}$  is bicubic upsampling, and  $\mathcal{E}(s_{S,b})$  is the prompt embedding of the sensor/band descriptor  $s_{S,b}$ .

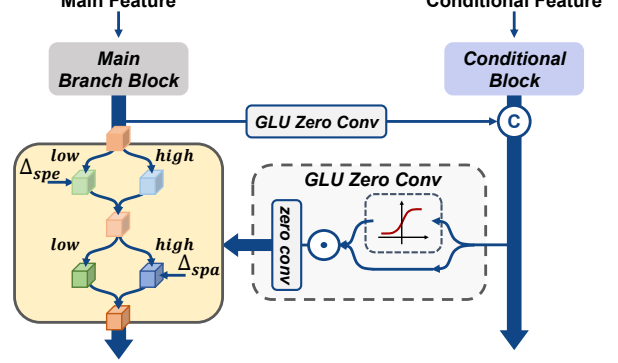


Figure 2. At each resolution, a PAN-driven spatial control branch and an LRMS-driven spectral control branch couple with the main trunk via GLU zero convolution residual adapters: bidirectional only in encoder, and branch→trunk in mid/decoder. Residuals are fused by Frequency-split injection (Sec. 3.4.1).

Given  $\hat{\boldsymbol{\epsilon}}^{(b)}$ , we compute the clean-latent estimate

$$\hat{\mathbf{z}}_0^{(b)} = \frac{\mathbf{z}_t^{(b)} - \sqrt{1 - \bar{\alpha}_t} \hat{\boldsymbol{\epsilon}}^{(b)}}{\sqrt{\bar{\alpha}_t}}. \quad (4)$$

#### 3.4.1. CONDITIONAL CONTROL MECHANISM

In Fig. 2, we introduce two lightweight control branches attached to a largely frozen SD-UNet trunk: a spatial branch conditioned on PAN  $\mathbf{P}$  and a spectral branch conditioned on  $\tilde{\mathbf{M}}^{(b)}$ . Each branch builds a multi-resolution feature pyramid  $\{\mathbf{s}_{\text{spa}}^\ell\}_\ell$  and  $\{\mathbf{s}_{\text{spe}}^\ell\}_\ell$  aligned with trunk resolutions. Let  $\mathbf{h}^\ell$  denote the trunk feature at resolution level  $\ell$ .

**Hybrid coupling.** At each resolution level  $\ell$ , the trunk  $\mathbf{h}^\ell$  and the branches  $\mathbf{s}_j^\ell$  ( $j \in \{\text{spa}, \text{spe}\}$ ) interact through lightweight residual adapters. We use bidirectional trunk↔branch interaction *only in the encoder*: the trunk first provides feedback to each branch, and each branch then returns a residual  $\Delta_j^\ell$  that is injected into the trunk. Concretely, for  $\ell \in \mathcal{L}_{\text{enc}}$ ,

$$\tilde{\mathbf{s}}_j^\ell = \Phi_j^\ell([\mathbf{s}_j^\ell, \Pi_{t \rightarrow j}^\ell(\mathbf{h}^\ell)]), \quad \Delta_j^\ell = \Pi_{j \rightarrow t}^\ell(\tilde{\mathbf{s}}_j^\ell), \quad (5)$$

where  $[\cdot, \cdot]$  is channel concatenation,  $\Phi_j^\ell$  is a narrow residual stack, and  $\Pi_{t \rightarrow j}^\ell / \Pi_{j \rightarrow t}^\ell$  are lightweight residual adapters.

In the *mid* and *decoder* blocks, we disable trunk→branch feedback and keep *unidirectional* branch→trunk control:

$$\tilde{\mathbf{s}}_j^\ell = \Phi_j^\ell(\mathbf{s}_j^\ell), \quad \Delta_j^\ell = \Pi_{j \rightarrow t}^\ell(\tilde{\mathbf{s}}_j^\ell). \quad (6)$$

This update is applied for all  $\ell \in \mathcal{L}_{\text{mid+dec}}$ , while Eq. (5) is used for  $\ell \in \mathcal{L}_{\text{enc}}$ , where  $\mathcal{L}_{\text{enc}}$  and  $\mathcal{L}_{\text{mid+dec}}$  denote the sets of encoder blocks and mid+decoder blocks, respectively.

To preserve the pretrained feature hierarchy, we initialize all coupling adapters to output zeros:

$$\Pi(\mathbf{x}) = \text{ZeroConv}_{1 \times 1}(\text{GLU}(\text{Conv}_{1 \times 1}(\mathbf{x}))), \quad (7)$$

where  $\text{ZeroConv}_{1 \times 1}$  is a  $1 \times 1$  convolution with zero-initialized weights. We use the standard gated linear unit: if  $\mathbf{u} = \text{Conv}_{1 \times 1}(\mathbf{x}) \in \mathbb{R}^{2C \times H \times W}$  and  $\mathbf{u} = [\mathbf{u}_1, \mathbf{u}_2]$  by channel split, then  $\text{GLU}(\mathbf{u}) = \mathbf{u}_1 \odot \sigma(\mathbf{u}_2)$  (Dauphin et al., 2017). This ensures  $\Pi(\mathbf{x}) = \mathbf{0}$  at initialization, keeping the pretrained trunk unchanged while allowing stable, gradual learning of task-specific control signals.

**Frequency-split injection.** PAN primarily provides sharp edges and fine spatial textures, while LRMS mainly constrains slowly-varying spectral radiometry (Vivone et al., 2020). We therefore fuse the branch-to-trunk residuals in the frequency domain by injecting *low-frequency* components from the spectral branch and *high-frequency* components from the spatial branch:

$$\mathbf{h}_1^\ell = \mathbf{h}^\ell + \lambda_{\text{spe}} \mathcal{L}(\Delta_{\text{spe}}^\ell), \quad (8)$$

$$\mathbf{h}_{\text{out}}^\ell = \mathbf{h}_1^\ell + \lambda_{\text{spa}} \mathcal{H}(\Delta_{\text{spa}}^\ell), \quad (9)$$

where  $\mathcal{L}(\cdot)$  is a fixed low-pass operator applied per-channel, and  $\mathcal{H}(\mathbf{x}) = \mathbf{x} - \mathcal{L}(\mathbf{x})$  denotes the corresponding high-pass residual. In our implementation,  $\mathcal{L}$  is a non-learned blur at each resolution level, so the split introduces no additional trainable parameters. We fix  $(\lambda_{\text{spe}}, \lambda_{\text{spa}}) = (1, 1)$  during training and optionally adjust them at inference to control the spectral–spatial trade-off (Appendix E.2).

**Metadata conditioning.** Different satellite sensors exhibit diverse spectral characteristics, making cross-sensor generalization challenging (Tuia et al., 2016). To address this, we condition the denoising network on sensor-aware metadata through text prompts. Each prompt  $s_{S,b}$  encodes the sensor name, band index, and wavelength range. We use a frozen pretrained CLIP text encoder to produce the embedding  $\mathcal{E}(s_{S,b})$ , which is injected into the pretrained UNet via standard cross-attention. To maintain training efficiency, we freeze the CLIP text encoder and the original pretrained UNet trunk weights, and only optimize lightweight sensor-conditioning parameters, including (i) the cross-attention projection matrices  $(W_Q, W_K, W_V)$  (Wu et al., 2023) and (ii) the parameters of the newly introduced control modules (e.g., control branches/adapters and RCBA).

#### 3.4.2. REGION-BASED CROSS-BAND ATTENTION

Although band-wise diffusion is computationally scalable, multispectral observations are not band-independent (Iqbal et al., 2021). For a fixed scene, responses across bands are jointly governed by shared physical factors, yielding strong cross-band correlations and characteristic spectral signatures (Wang et al., 2017). Denoising bands independently may therefore cause band drift. To restore inter-band consistency while retaining the efficiency of band-wise modeling, we introduce a lightweight *Region-based Cross-Band Attention* (RCBA) module, inserted only at the mid-block of

the conditional branch to minimally perturb the pretrained prior. In practice, we regroup bands from the same scene and apply attention over the band axis.

Let  $\mathbf{F} \in \mathbb{R}^{(NB) \times C \times H' \times W'}$  denote the mid-block feature after folding the band dimension into the batch dimension, where  $N$  is the number of scenes in a minibatch,  $B$  is the number of spectral bands, and  $C$  is the feature channel dimension. We reshape it to  $\bar{\mathbf{F}} \in \mathbb{R}^{N \times B \times C \times H' \times W'}$ . RCBA follows a region-based formulation; for efficiency we use a single global region ( $R=1$ ) and summarize each band by global average pooling (GAP):

$$\begin{aligned} \mathbf{u}_{n,b} &= \text{GAP}(\bar{\mathbf{F}}_{n,b}), \\ \mathbf{U}_n &= [\mathbf{u}_{n,1}, \dots, \mathbf{u}_{n,B}]. \end{aligned} \quad (10)$$

We then apply multi-head self-attention over the band dimension to obtain cross-band corrected tokens:

$$\mathbf{U}'_n = \text{MHSA}(\text{LN}(\mathbf{U}_n)) \in \mathbb{R}^{B \times C}. \quad (11)$$

The correction is projected and broadcast back to the feature maps as a residual:

$$\bar{\mathbf{F}}'_{n,b} = \bar{\mathbf{F}}_{n,b} + \eta \cdot \text{Broadcast}(W_{\text{out}}(\mathbf{U}'_n[b])). \quad (12)$$

where  $\text{Broadcast}(\cdot)$  expands a  $C$ -dim vector to  $C \times H' \times W'$  by replication,  $W_{\text{out}} : \mathbb{R}^C \rightarrow \mathbb{R}^C$  is a linear projection, and  $\eta$  is a learnable scalar. We initialize  $\eta = 0$  and  $W_{\text{out}} = \mathbf{0}$  so that RCBA starts as an identity mapping and does not change the pretrained trunk activations at initialization. Finally, we reshape  $\bar{\mathbf{F}}'$  back to  $(NB) \times C \times H' \times W'$ .

## 4. Experiments

### 4.1. Experimental Setup

**Datasets.** We conduct experiments on the PanCollection benchmark (Deng et al., 2022), which provides co-registered PAN/MS image pairs from four satellite sensors: Quick-Bird (QB,  $B=4$ ), WorldView-3 (WV3,  $B=8$ ), WorldView-2 (WV2,  $B=8$ ), and GaoFen-2 (GF2,  $B=4$ ). All sensors have a spatial resolution ratio of  $r=4$ . PanCollection includes both reduced-resolution (ReducedData) and full-resolution (FullData) test sets, with 20 test samples per sensor in each setting. We use ReducedData for reference-based evaluation following the standard Wald protocol, and FullData for real-world testing with no-reference metrics (Appendix D.2). WV2 is provided as a held-out test set and is used to evaluate cross-sensor generalization capability. We report quantitative results on WV3 and QB as representative cases for 8-band and 4-band sensors, respectively, and provide complete results for all four sensors in Appendix F.

**Baselines and fairness.** We compare our method with the following two groups of methods: (1) **Deep-learning**

Table 1. Quantitative results on the WorldView-3 (WV3) dataset. Best and second-best results are in **bold** and underlined.

METHODS		REDUCED RESOLUTION				FULL RESOLUTION		
MODELS	PUB/YEAR	$Q_8 \uparrow$	$SAM \downarrow$	$ERGAS \downarrow$	$SCC \uparrow$	$D_\lambda \downarrow$	$D_s \downarrow$	$HQNR \uparrow$
PANNET	ICCV'17	$0.891 \pm 0.045$	$3.613 \pm 0.787$	$2.664 \pm 0.347$	$0.943 \pm 0.018$	$0.017 \pm 0.008$	$0.047 \pm 0.014$	$0.937 \pm 0.015$
FUSIONNET	TGRS'20	$0.904 \pm 0.092$	$3.324 \pm 0.411$	$2.465 \pm 0.603$	$0.958 \pm 0.023$	$0.024 \pm 0.011$	$0.036 \pm 0.016$	$0.940 \pm 0.019$
LAGCONV	AAAI'22	$0.910 \pm 0.114$	$3.104 \pm 1.119$	$2.300 \pm 0.911$	$0.980 \pm 0.043$	$0.036 \pm 0.009$	$0.032 \pm 0.016$	$0.934 \pm 0.011$
BiMPAN	ACMM'23	$0.915 \pm 0.087$	$2.984 \pm 0.601$	$2.257 \pm 0.552$	$0.984 \pm 0.005$	$0.017 \pm 0.019$	$0.035 \pm 0.015$	$0.949 \pm 0.026$
ARCONV	CVPR'25	$0.916 \pm 0.083$	$2.858 \pm 0.590$	$2.117 \pm 0.528$	$0.989 \pm 0.014$	$0.014 \pm 0.006$	$0.030 \pm 0.007$	$0.958 \pm 0.010$
WFANET	AAAI'25	$0.917 \pm 0.088$	$2.855 \pm 0.618$	$2.095 \pm 0.422$	$0.989 \pm 0.011$	$0.012 \pm 0.007$	$0.031 \pm 0.009$	$0.957 \pm 0.010$
PANDIFF	TGRS'23	$0.898 \pm 0.090$	$3.297 \pm 0.235$	$2.467 \pm 0.166$	$0.980 \pm 0.019$	$0.027 \pm 0.108$	$0.054 \pm 0.047$	$0.920 \pm 0.077$
SSDIFF	NEURIPS'24	$0.915 \pm 0.086$	$2.843 \pm 0.529$	$2.106 \pm 0.416$	$0.986 \pm 0.004$	$0.013 \pm 0.005$	$0.031 \pm 0.003$	$0.956 \pm 0.016$
SGDIFF	CVPR'25	$0.921 \pm 0.082$	$2.771 \pm 0.511$	$2.044 \pm 0.449$	$0.987 \pm 0.009$	$0.012 \pm 0.005$	$0.027 \pm 0.003$	$0.960 \pm 0.006$
<b>SALAD-PAN</b>		<b><math>0.924 \pm 0.064</math></b>	<b><math>2.689 \pm 0.135</math></b>	<b><math>1.839 \pm 0.211</math></b>	<b><math>0.989 \pm 0.007</math></b>	<b><math>0.010 \pm 0.008</math></b>	<b><math>0.021 \pm 0.004</math></b>	<b><math>0.965 \pm 0.007</math></b>

 Table 2. Quantitative results on the QuickBird (QB) dataset. Best and second-best results are in **bold** and underlined.

METHODS		REDUCED RESOLUTION				FULL RESOLUTION		
MODELS	PUB/YEAR	$Q_4 \uparrow$	$SAM \downarrow$	$ERGAS \downarrow$	$SCC \uparrow$	$D_\lambda \downarrow$	$D_s \downarrow$	$HQNR \uparrow$
PANNET	ICCV'17	$0.885 \pm 0.118$	$5.791 \pm 0.995$	$5.863 \pm 0.413$	$0.948 \pm 0.021$	$0.059 \pm 0.017$	$0.061 \pm 0.010$	$0.883 \pm 0.025$
FUSIONNET	TGRS'20	$0.925 \pm 0.087$	$4.923 \pm 0.812$	$4.159 \pm 0.351$	$0.956 \pm 0.018$	$0.059 \pm 0.019$	$0.052 \pm 0.009$	$0.892 \pm 0.022$
LAGCONV	AAAI'22	$0.916 \pm 0.130$	$4.370 \pm 0.720$	$3.740 \pm 0.290$	$0.959 \pm 0.047$	$0.085 \pm 0.024$	$0.068 \pm 0.014$	$0.853 \pm 0.018$
BiMPAN	ACMM'23	$0.931 \pm 0.091$	$4.586 \pm 0.821$	$3.840 \pm 0.319$	$0.980 \pm 0.008$	$0.026 \pm 0.020$	$0.040 \pm 0.013$	$0.935 \pm 0.030$
ARCONV	CVPR'25	$0.936 \pm 0.088$	$4.453 \pm 0.499$	$3.649 \pm 0.401$	<b><math>0.987 \pm 0.009</math></b>	<b><math>0.019 \pm 0.014</math></b>	$0.034 \pm 0.017$	$0.948 \pm 0.042$
WFANET	AAAI'25	$0.935 \pm 0.092$	$4.490 \pm 0.582$	$3.604 \pm 0.337$	$0.986 \pm 0.008$	$0.019 \pm 0.016$	$0.033 \pm 0.019$	$0.948 \pm 0.037$
PANDIFF	TGRS'23	$0.934 \pm 0.095$	$4.575 \pm 0.255$	$3.742 \pm 0.353$	$0.980 \pm 0.007$	$0.058 \pm 0.015$	$0.064 \pm 0.020$	$0.881 \pm 0.075$
SSDIFF	NEURIPS'24	$0.934 \pm 0.094$	$4.464 \pm 0.747$	$3.632 \pm 0.275$	$0.982 \pm 0.008$	$0.031 \pm 0.011$	$0.036 \pm 0.013$	$0.934 \pm 0.021$
SGDIFF	CVPR'25	$0.938 \pm 0.087$	<u><math>4.353 \pm 0.741</math></u>	<u><math>3.578 \pm 0.290</math></u>	$0.983 \pm 0.007$	$0.023 \pm 0.013$	$0.043 \pm 0.012$	$0.934 \pm 0.011$
<b>SALAD-PAN</b>		<b><math>0.939 \pm 0.088</math></b>	<b><math>4.198 \pm 0.526</math></b>	<b><math>3.251 \pm 0.288</math></b>	$0.984 \pm 0.009$	<b><math>0.017 \pm 0.011</math></b>	<b><math>0.026 \pm 0.009</math></b>	<b><math>0.957 \pm 0.010</math></b>

**models** built upon feed-forward fusion and feature aggregation designs, including PanNet (Yang et al., 2017), FusionNet (Deng et al., 2020), LAGConv (Jin et al., 2022), BiMPan (Hou et al., 2023), ARConv (Wang et al., 2025), and WFANet (Huang et al., 2025b). (2) **Diffusion-based** generative restoration baselines, including PanDiff (Meng et al., 2023), SSDiff (Zhong et al., 2024), and SGDiff (Xing et al., 2025) (Appendix D). Whenever possible, we use official implementations and released checkpoints. If pretrained weights are unavailable, we retrain the baselines on the same training split using the same RR degradation pipeline and identical inputs. All methods are evaluated under the unified preprocessing and postprocessing described above, ensuring that observed differences mainly stem from model design and learning strategy rather than data handling.

**Evaluation metrics.** Following common practice in pan-sharpening evaluation, we assess performance under both reduced-resolution (RR) and full-resolution (FR) settings. On ReducedData (RR) under the Wald protocol, we report full-reference metrics that jointly measure spectral fidelity and spatial-detail preservation. Specifically, we adopt multi-band  $Q_4/Q_8$  ( $Q_4$  for 4-band sensors and  $Q_8$  for 8-band sensors) (Alparone et al., 2004; Garzelli & Nencini, 2009) as an overall quality indicator for multispectral fusion. We further use SAM and ERGAS (lower is better) to quantify

spectral discrepancies: SAM measures the angular deviation between the fused image and the reference, while ERGAS captures the global radiometric error normalized by dynamic range (Yuhas et al., 1992; Wald, 2000). To evaluate spatial-structure preservation, we report SCC (higher is better), which reflects the correlation of spatial details between the fused result and the reference (Zhou et al., 1998). On FullData (FR) for real-world testing where no ground-truth HRMS is available, we follow the widely used HQNR/QNR protocol (Alparone et al., 2008; Aiazzi et al., 2014; Arienzo et al., 2022). We report  $D_\lambda$  and  $D_s$  (both lower is better), where  $D_\lambda$  measures spectral distortion between LRMS and the fused HRMS, and  $D_s$  measures spatial distortion with respect to the PAN image. HQNR (higher is better) is a composite no-reference score that summarizes overall quality by jointly accounting for spectral and spatial degradations.

**Implementation details.** We implement SALAD-Pan in PyTorch and train for 100k steps using AdamW (Loshchilov & Hutter, 2017) with learning rate  $2 \times 10^{-4}$  and batch size  $N=24$ . To enable band-wise processing with a unified single-channel backbone, we reshape each input batch from  $(N, B, H, W)$  to  $(NB, 1, H, W)$  by folding the spectral dimension into the batch dimension, yielding an effective single-channel batch size of  $NB$ . Since the number of bands  $B$  varies across sensors (GF2/QB:  $B=4$ ; WV2/WV3:

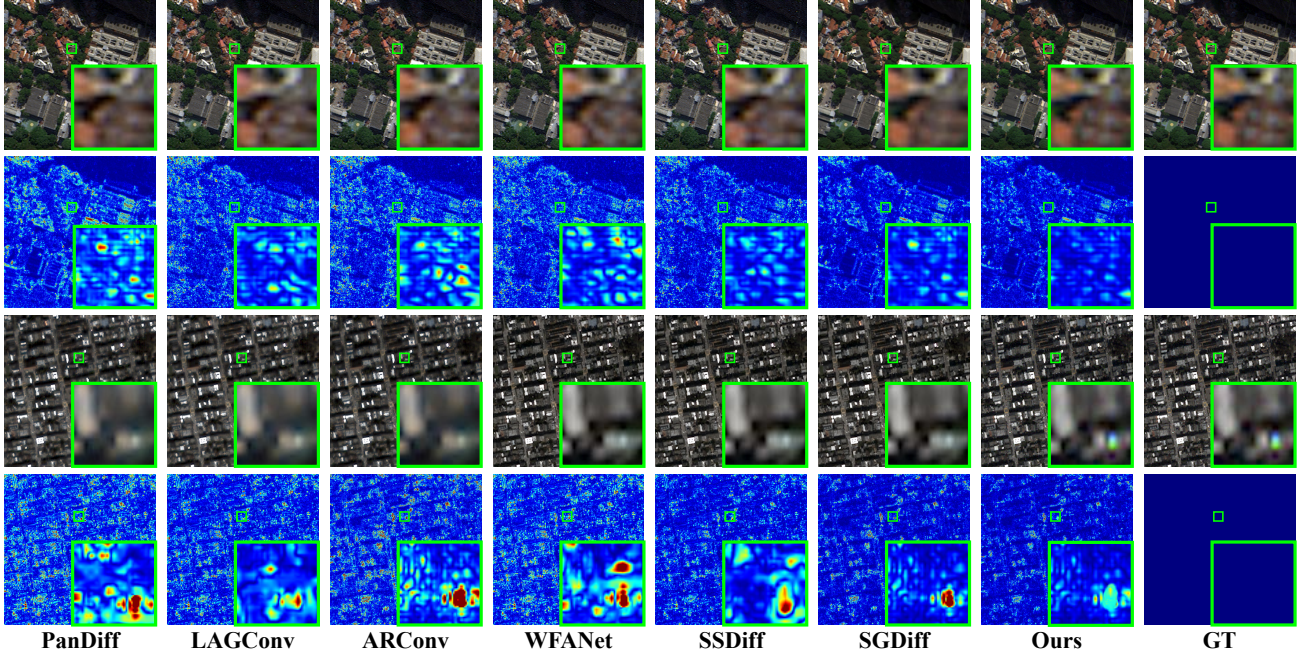


Figure 3. Visual comparison on WorldView-3 (WV-3) and QuickBird (QB) dataset at reduced resolution (RR).

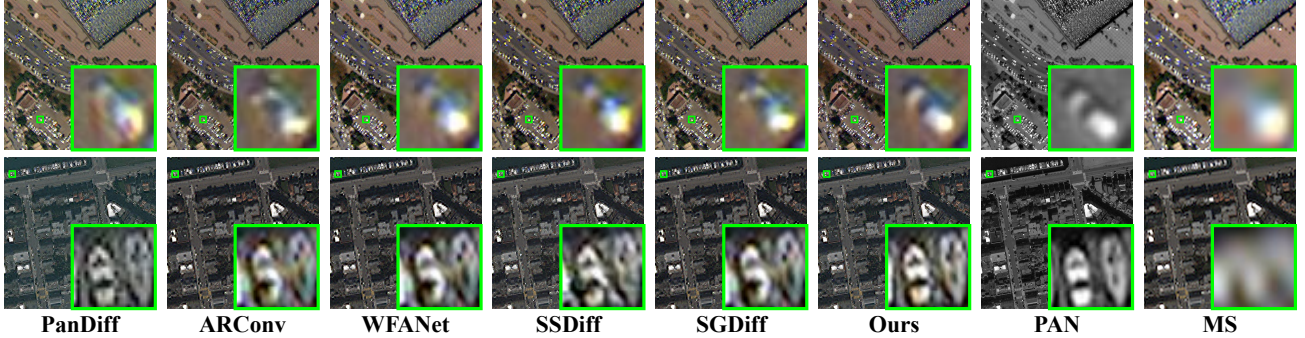


Figure 4. Visual comparison on WorldView-3 (WV-3) and QuickBird (QB) dataset at full resolution (FR).

$B=8$ ), each optimization step samples data from a single sensor so that  $B$  is constant within the step. For joint training across sensors, we adopt a round-robin scheduler that cycles through sensor datasets while sharing all trainable parameters across sensors. All experiments are conducted on an RTX 4090 GPU. During inference, we use the UniPC sampler (Zhao et al., 2023) with  $K=20$  sampling steps.

## 4.2. Main Results

**Quantitative results (RR and FR).** Tables 1 and 2 report results on WV3 and QB under reduced-resolution (RR) and full-resolution (FR) settings (Deng et al., 2022). **RR** (Wald/ReducedData): SALAD-Pan achieves the strongest overall performance, reducing spectral distortion (SAM/ERGAS) while maintaining high structural fidelity ( $Q_4/Q_8$  and SCC). For example, on WV3 our ERGAS

reaches 1.839 while structural metrics remain competitive.

**FR** (FullData): Under native acquisitions where no reference HRMS is available, SALAD-Pan attains the highest HQNR and also yields lower  $D_\lambda$  and  $D_s$ , indicating reduced spectral and spatial distortions; e.g., HQNR is 0.965 on WV3. All methods use identical preprocessing, resizing, and border handling; therefore, the improvements are attributable to the proposed model rather than differences in data processing.

**Qualitative comparison.** Figures 3 and 4 show representative visual comparisons. **RR:** In Fig. 3, the zoomed-in regions (green boxes) emphasize thin structures and sharp boundaries. SALAD-Pan produces cleaner edges with fewer color fringes, and the error heatmaps show fewer high-error responses around boundaries and textured areas, suggesting reduced artifacts while recovering fine details. **FR:** In Fig. 4,

SALAD-Pan yields spatial details that align better with the PAN reference in the zoom-ins while preserving the global chromaticity suggested by the MS input, avoiding over-sharpening and local color shifts seen in competing methods. In particular, in the WV3 FR vehicle example, SALAD-Pan better preserves the car silhouette and boundary contrast, with reduced blurring and color bleeding, whereas other methods often smear the vehicle shape or introduce noticeable halos. All visualizations use the same band-to-RGB mapping and identical contrast stretching across methods.

### 4.3. Cross-Sensor Generalization and Efficiency

**Zero-shot cross-sensor transfer.** We evaluate generalization across sensors in a strict zero-shot setting. A single SALAD-Pan model is jointly trained on GF2, QB, and WV3, and then directly tested on the unseen WV2 sensor without any WV2-specific fine-tuning or model selection. To accommodate different numbers of spectral bands, we use single-sensor mini-batches during joint training while sharing one set of model parameters; at test time, the inference pipeline remains unchanged. As shown in Table 3, SALAD-Pan improves transfer performance on WV2 with lower SAM (4.968→4.689) and higher  $Q_8$  than competing methods, while remaining competitive on ERGAS.

Table 3. Zero-shot cross-sensor transfer to WorldView-2 (WV2) under the reduced-resolution (RR) protocol.

METHODS	SAM $\downarrow$	ERGAS $\downarrow$	$Q_8 \uparrow$
FUSIONNET	6.426 $\pm$ 0.860	5.136 $\pm$ 0.515	0.796 $\pm$ 0.074
LAGCONV	6.955 $\pm$ 0.474	5.326 $\pm$ 0.319	0.806 $\pm$ 0.084
BIMPAN	5.328 $\pm$ 0.502	4.207 $\pm$ 0.448	0.837 $\pm$ 0.074
SSDIFF	5.065 $\pm$ 0.564	3.989 $\pm$ 0.430	0.858 $\pm$ 0.078
WFANET	5.715 $\pm$ 0.544	4.380 $\pm$ 0.466	0.845 $\pm$ 0.080
SGDIFF	4.968 $\pm$ 0.511	<b>3.868<math>\pm</math>0.449</b>	0.858 $\pm$ 0.082
<b>SALAD-PAN</b>	<b>4.689<math>\pm</math>0.453</b>	3.910 $\pm$ 0.332	<b>0.874<math>\pm</math>0.077</b>

**Efficiency analysis.** We benchmark inference efficiency under a unified setup on a single RTX 4090 GPU with batch size of one. Latency is reported as wall-clock time per reconstructed image and includes generating all spectral bands, while excluding data loading and external pre/post-processing; we also report the number of function evaluations (NFE) (Lu et al., 2022), where one denoiser forward pass counts as one NFE. Table 4 summarizes the quality-speed trade-off on QB under the reduced-resolution protocol. SALAD-Pan achieves stronger restoration quality with a modest sampling budget and improves latency, using 20 NFE with 3.36 seconds per image, whereas diffusion baselines typically require heavier sampling and run slower under comparable settings. Overall, these results validate that performing diffusion in the compact latent space, together with band-wise processing, substantially improves inference efficiency while preserving reconstruction quality.

Table 4. Efficiency comparison on QB under the reduced-resolution (RR) protocol.

METHODS	SAM $\downarrow$	ERGAS $\downarrow$	NFE	LATENCY (S)
PANDIFF	4.575 $\pm$ 0.255	3.742 $\pm$ 0.353	1000	356.63 $\pm$ 1.98
SSDIFF	4.464 $\pm$ 0.747	3.632 $\pm$ 0.275	10	10.10 $\pm$ 0.21
SGDIFF	4.353 $\pm$ 0.741	3.578 $\pm$ 0.290	50	6.64 $\pm$ 0.09
<b>SALAD-PAN</b>	<b>4.198<math>\pm</math>0.526</b>	<b>3.251<math>\pm</math>0.288</b>	20	<b>3.36<math>\pm</math>0.07</b>

### 4.4. Ablation Studies

We conduct ablation studies on WV3 under the reduced-resolution protocol with identical training data and inference settings. Table 5 starts from a single-branch baseline (Cond.=1B) and progressively adds our design choices. Moving from single-branch to dual-branch conditioning (Cond.=2B) consistently improves the metrics, supporting the benefit of disentangling PAN-driven spatial guidance and LRMS-driven spectral guidance. Adding metadata prompts (PR) further enhances spectral consistency by providing sensor- and band-aware priors. Finally, incorporating RCBA yields the best overall performance, indicating that explicit cross-band interaction helps maintain inter-band coherence under band-wise processing.

Table 5. Ablation on WV3 (RR). Cond.: 1B/2B = single-/dual-branch; all 2B variants use frequency-split injection (Sec. 3.4.1). PR: metadata prompts. RCBA: region-based cross-band attention (Sec. 3.4.2).

COND.	PR	RCBA	SAM $\downarrow$	ERGAS $\downarrow$
1B	–	–	3.057 $\pm$ 0.195	2.110 $\pm$ 0.245
2B	–	–	2.809 $\pm$ 0.135	2.045 $\pm$ 0.192
2B	✓	–	2.782 $\pm$ 0.141	1.994 $\pm$ 0.300
2B	✓	✓	<b>2.689<math>\pm</math>0.135</b>	<b>1.839<math>\pm</math>0.211</b>

## 5. Conclusion

We propose SALAD-Pan, a sensor-agnostic latent diffusion framework for efficient pansharpening. We train a band-wise single-channel VAE to perform diffusion in a compact latent space, significantly reducing computational cost compared to prior pixel-space diffusion methods and naturally adapting to arbitrary spectral band configurations across sensors through its band-wise design. We further introduce a disentangled spatial-spectral conditioning mechanism with bidirectional interaction, where PAN, LRMS, and sensor-aware text prompts jointly guide diffusion, along with a lightweight Region-based Cross-Band Attention module that enhances cross-modal fusion and spectral consistency. Extensive experiments on GaoFen-2, QuickBird, and WorldView-3 datasets demonstrate consistent state-of-the-art performance with 2–3 $\times$  faster inference and strong zero-shot cross-sensor generalization, highlighting latent diffusion as a deployable solution for pansharpening.

## Impact Statement

This paper presents work whose goal is to advance the field of Machine Learning. There are many potential societal consequences of our work, none which we feel must be specifically highlighted here.

## References

- Aiazzi, B., Alparone, L., Baronti, S., Carlà, R., Garzelli, A., and Santurri, L. Full-scale assessment of pansharpening methods and data products. In *Image and signal processing for remote sensing XX*, volume 9244, pp. 924402. SPIE, 2014.
- Alparone, L., Baronti, S., Garzelli, A., and Nencini, F. A global quality measurement of pan-sharpened multispectral imagery. *IEEE Geoscience and Remote Sensing Letters*, 1(4):313–317, 2004.
- Alparone, L., Aiazzi, B., Baronti, S., Garzelli, A., Nencini, F., and Selva, M. Multispectral and panchromatic data fusion assessment without reference. *Photogrammetric Engineering & Remote Sensing*, 74(2):193–200, 2008.
- Arienzo, A., Vivone, G., Garzelli, A., Alparone, L., and Chanussot, J. Full-resolution quality assessment of pan-sharpening: Theoretical and hands-on approaches. *IEEE Geoscience and Remote Sensing Magazine*, 10(3):168–201, 2022.
- Cao, Z., Cao, S., Deng, L.-J., Wu, X., Hou, J., and Vivone, G. Diffusion model with disentangled modulations for sharpening multispectral and hyperspectral images. *Information Fusion*, 104:102158, 2024.
- Cao, Z., Zhong, Y., and Deng, L.-J. Taming flow matching with unbalanced optimal transport into fast pansharpening. *arXiv preprint arXiv:2503.14975*, 2025.
- Ciotola, M., Vitale, S., Mazza, A., Poggi, G., and Scarpa, G. Pansharpening by convolutional neural networks in the full resolution framework. *IEEE Transactions on Geoscience and Remote Sensing*, 60:1–17, 2022.
- Dauphin, Y. N., Fan, A., Auli, M., and Grangier, D. Language modeling with gated convolutional networks. In *International conference on machine learning*, pp. 933–941. PMLR, 2017.
- Deng, L.-J., Vivone, G., Jin, C., and Chanussot, J. Detail injection-based deep convolutional neural networks for pansharpening. *IEEE Transactions on Geoscience and Remote Sensing*, 59(8):6995–7010, 2020.
- Deng, L.-J., Vivone, G., Paoletti, M. E., Scarpa, G., He, J., Zhang, Y., Chanussot, J., and Plaza, A. Machine learning in pansharpening: A benchmark, from shallow to deep networks. *IEEE Geoscience and Remote Sensing Magazine*, 10(3):279–315, 2022.
- Dong, R., Mou, L., Chen, M., Li, W., Tong, X.-Y., Yuan, S., Zhang, L., Zheng, J., Zhu, X., and Fu, H. Large-scale land cover mapping with fine-grained classes via class-aware semi-supervised semantic segmentation. In *Proceedings of the IEEE/CVF International Conference on Computer Vision*, pp. 16783–16793, 2023.
- Duran, J., Buades, A., Coll, B., Sbert, C., and Blanchet, G. A survey of pansharpening methods with a new band-decoupled variational model. *ISPRS Journal of Photogrammetry and Remote Sensing*, 125:78–105, 2017.
- Garzelli, A. and Nencini, F. Hypercomplex quality assessment of multi/hyperspectral images. *IEEE Geoscience and Remote Sensing Letters*, 6(4):662–665, 2009.
- Ho, J., Jain, A., and Abbeel, P. Denoising diffusion probabilistic models. *Advances in neural information processing systems*, 33:6840–6851, 2020.
- Hou, J., Cao, Q., Ran, R., Liu, C., Li, J., and Deng, L.-J. Bidomain modeling paradigm for pansharpening. In *Proceedings of the 31st ACM international conference on multimedia*, pp. 347–357, 2023.
- Huang, J., Chen, H., Ren, J., Peng, S., and Deng, L. A general adaptive dual-level weighting mechanism for remote sensing pansharpening. In *Proceedings of the Computer Vision and Pattern Recognition Conference*, pp. 7447–7456, 2025a.
- Huang, J., Huang, R., Xu, J., Peng, S., Duan, Y., and Deng, L.-J. Wavelet-assisted multi-frequency attention network for pansharpening. *Proceedings of the AAAI Conference on Artificial Intelligence*, 39(4):3662–3670, 2025b.
- Iqbal, I. M., Balzter, H., and Shabbir, A. Identifying the spectral signatures of invasive and native plant species in two protected areas of pakistan through field spectroscopy. *Remote Sensing*, 13(19):4009, 2021.
- Javan, F. D., Samadzadegan, F., Mehravar, S., Toosi, A., Khatami, R., and Stein, A. A review of image fusion techniques for pan-sharpening of high-resolution satellite imagery. *ISPRS journal of photogrammetry and remote sensing*, 171:101–117, 2021.
- Jin, Z.-R., Zhang, T.-J., Jiang, T.-X., Vivone, G., and Deng, L.-J. Lagconv: Local-context adaptive convolution kernels with global harmonic bias for pansharpening. *Proceedings of the AAAI Conference on Artificial Intelligence*, 36(1):1113–1121, 2022.
- Kalluri, T., Lee, J., Sohn, K., Singla, S., Chandraker, M., Xu, J., and Liu, J. Robust disaster assessment from aerial

- imagery using text-to-image synthetic data. In *Proceedings of the Computer Vision and Pattern Recognition Conference*, pp. 7449–7459, 2024.
- Kawar, B., Elad, M., Ermon, S., and Song, J. Denoising diffusion restoration models. *Advances in neural information processing systems*, 35:23593–23606, 2022.
- Kim, S., Do, J., Lee, J., and Kim, M. U-know-diffpan: An uncertainty-aware knowledge distillation diffusion framework with details enhancement for pan-sharpening. In *Proceedings of the Computer Vision and Pattern Recognition Conference*, pp. 23069–23079, 2025.
- Loshchilov, I. and Hutter, F. Decoupled weight decay regularization. *arXiv preprint arXiv:1711.05101*, 2017.
- Lu, C., Zhou, Y., Bao, F., Chen, J., Li, C., and Zhu, J. Dpm-solver: A fast ode solver for diffusion probabilistic model sampling in around 10 steps. *Advances in neural information processing systems*, 35:5775–5787, 2022.
- Ma, M., Jiang, Y., Zhao, M., Li, J., and Zhang, W. Hetssnet: Spatial-spectral heterogeneous graph learning network for panchromatic and multispectral images fusion. *arXiv preprint arXiv:2502.04623*, 2025.
- Masi, G., Cozzolino, D., Verdoliva, L., and Scarpa, G. Pan-sharpening by convolutional neural networks. *Remote Sensing*, 8(7):594, 2016.
- Meng, Q., Shi, W., Li, S., and Zhang, L. Pandiff: A novel pansharpening method based on denoising diffusion probabilistic model. *IEEE Transactions on Geoscience and Remote Sensing*, 61:1–17, 2023.
- Nunez, J., Otazu, X., Fors, O., Prades, A., Pala, V., and Arbiol, R. Multiresolution-based image fusion with additive wavelet decomposition. *IEEE Transactions on Geoscience and Remote sensing*, 37(3):1204–1211, 2002.
- Radford, A., Kim, J. W., Hallacy, C., Ramesh, A., Goh, G., Agarwal, S., Sastry, G., Askell, A., Mishkin, P., Clark, J., et al. Learning transferable visual models from natural language supervision. In *International conference on machine learning*, pp. 8748–8763. PMLR, 2021.
- Rombach, R., Blattmann, A., Lorenz, D., Esser, P., and Ommer, B. High-resolution image synthesis with latent diffusion models. In *Proceedings of the Computer Vision and Pattern Recognition Conference*, pp. 10684–10695, 2022.
- Tuia, D., Marcos, D., and Camps-Valls, G. Multi-temporal and multi-source remote sensing image classification by nonlinear relative normalization. *ISPRS Journal of Photogrammetry and Remote Sensing*, 120:1–12, 2016.
- Vivone, G., Alparone, L., Chanussot, J., Dalla Mura, M., Garzelli, A., Licciardi, G. A., Restaino, R., and Wald, L. A critical comparison among pansharpening algorithms. *IEEE Transactions on Geoscience and Remote Sensing*, 53(5):2565–2586, 2014.
- Vivone, G., Restaino, R., and Chanussot, J. A bayesian procedure for full-resolution quality assessment of pan-sharpened products. *IEEE Transactions on Geoscience and Remote Sensing*, 56(8):4820–4834, 2018.
- Vivone, G., Marano, S., and Chanussot, J. Pansharpening: Context-based generalized laplacian pyramids by robust regression. *IEEE Transactions on Geoscience and Remote Sensing*, 58(9):6152–6167, 2020.
- Vivone, G., Deng, L.-J., Deng, S., Hong, D., Jiang, M., Li, C., Li, W., Shen, H., Wu, X., Xiao, J.-L., et al. Deep learning in remote sensing image fusion: Methods, protocols, data, and future perspectives. *IEEE Geoscience and Remote Sensing Magazine*, 2024.
- Wald, L. Quality of high resolution synthesised images: Is there a simple criterion? In *Third conference "Fusion of Earth data: merging point measurements, raster maps and remotely sensed images"*, pp. 99–103. SEE/URISCA, 2000.
- Wald, L., Ranchin, T., and Mangolini, M. Fusion of satellite images of different spatial resolutions: Assessing the quality of resulting images. *Photogrammetric engineering and remote sensing*, 63(6):691–699, 1997.
- Wang, H. and Wu, M. Urban change detection of remote sensing images via deep-feature extraction. *Scientific Reports*, 15(1):21473, 2025.
- Wang, X., Zheng, Z., Shao, J., Duan, Y., and Deng, L.-J. Adaptive rectangular convolution for remote sensing pansharpening. In *Proceedings of the Computer Vision and Pattern Recognition Conference*, pp. 17872–17881, 2025.
- Wang, Y., Chen, X., Han, Z., and He, S. Hyperspectral image super-resolution via nonlocal low-rank tensor approximation and total variation regularization. *Remote Sensing*, 9(12):1286, 2017.
- Wu, J. Z., Ge, Y., Wang, X., Lei, S. W., Gu, Y., Shi, Y., Hsu, W., Shan, Y., Qie, X., and Shou, M. Z. Tune-a-video: One-shot tuning of image diffusion models for text-to-video generation. In *Proceedings of the IEEE/CVF international conference on computer vision*, pp. 7623–7633, 2023.
- Wu, R., Zhang, Z., Deng, S., Duan, Y., and Deng, L.-J. Panadapter: Two-stage fine-tuning with spatial-spectral priors injecting for pansharpening. In *Proceedings of the*

- AAAI Conference on Artificial Intelligence, volume 39, pp. 8450–8459, Palo Alto, CA, USA, 2025. Association for the Advancement of Artificial Intelligence.
- Xing, Y., Qu, L., Zhang, S., Feng, J., Zhang, X., and Zhang, Y. Empower generalizability for pancharpening through text-modulated diffusion model. *IEEE Transactions on Geoscience and Remote Sensing*, 2024a.
- Xing, Y., Qu, L., Zhang, S., Zhang, K., Zhang, Y., and Bruzzone, L. Crossdiff: Exploring self-supervised representation of pancharpening via cross-predictive diffusion model. *IEEE Transactions on Image Processing*, 2024b.
- Xing, Y., Qu, L., Zhang, S., Xu, D., Yang, Y., and Zhang, Y. Dual-granularity semantic guided sparse routing diffusion model for general pancharpening. In *Proceedings of the Computer Vision and Pattern Recognition Conference*, pp. 12658–12668, 2025.
- Yang, J., Fu, X., Hu, Y., Huang, Y., Ding, X., and Paisley, J. Pannet: A deep network architecture for pan-sharpening. In *Proceedings of the IEEE international conference on computer vision*, pp. 5449–5457, 2017.
- Yuhas, R. H., Goetz, A. F., and Boardman, J. W. Discrimination among semi-arid landscape endmembers using the spectral angle mapper (sam) algorithm. In *JPL, Summaries of the Third Annual JPL Airborne Geoscience Workshop. Volume 1: AVIRIS Workshop*, 1992.
- Zhang, J., Fang, F., Wang, T., Zhang, G., and Song, H. Frdiff: Framelet-based conditional diffusion model for multispectral and panchromatic image fusion. *IEEE Transactions on Multimedia*, 2025.
- Zhang, K., Zhang, F., Wan, W., Yu, H., Sun, J., Del Ser, J., Elyan, E., and Hussain, A. Panchromatic and multispectral image fusion for remote sensing and earth observation: Concepts, taxonomy, literature review, evaluation methodologies and challenges ahead. *Information Fusion*, 93:227–242, 2023.
- Zhao, W., Bai, L., Rao, Y., Zhou, J., and Lu, J. Unipc: A unified predictor-corrector framework for fast sampling of diffusion models. *Advances in Neural Information Processing Systems*, 36:49842–49869, 2023.
- Zhong, Y., Wu, X., Cao, Z., Dou, H.-X., and Deng, L.-J. Ssdiff: Spatial-spectral integrated diffusion model for remote sensing pancharpening. *Advances in Neural Information Processing Systems*, 37:77962–77986, 2024.
- Zhou, H., Liu, Q., and Wang, Y. Panformer: A transformer based model for pan-sharpening. In *2022 IEEE international conference on multimedia and expo (ICME)*, pp. 1–6. IEEE, 2022.
- Zhou, J., Civco, D. L., and Silander, J. A. A wavelet transform method to merge landsat tm and spot panchromatic data. *International journal of remote sensing*, 19(4):743–757, 1998.

## A. Appendix Outline

This supplementary material complements the main paper by providing (i) further analysis of sensor-induced PAN–MS coupling shifts that motivate our design, (ii) fully reproducible datasets, protocols, metrics, and implementation details, and (iii) complete per-sensor results and additional visual comparisons for SALAD-PAN. It is organized as follows:

- **Notation summary (App. A.1).** We provide a concise glossary of symbols covering data and resolution variables, Stage-I VAE components and latent scaling, Stage-II diffusion variables and objectives, and conditioning and control modules, to ease cross-referencing.
- **Inductive biases for cross-sensor PAN–MS coupling (App. B).** We analyze two sources of cross-sensor shift. The first is sensor-dependent PAN–MS spectral mixing, supported by per-sensor linear PAN surrogates in Fig. 5. The second is the RR→FR mismatch in high frequencies, quantified by band-wise correlation shifts in Fig. 6. These findings motivate our band-wise formulation and frequency-split conditioning.
- **Datasets and protocols (App. C).** We describe the PanCollection format, sensor and band configurations, patch and image sizes, and strict train, validation, and test splits in Table 6. We also specify the joint-training and zero-shot settings, and the RR ReducedData and FR FullData evaluation protocols.
- **Evaluation setup (App. D).** We enumerate all compared methods in App. D.1. We then provide exact definitions and computation details for RR full-reference metrics, including Q4 or Q8, SAM, ERGAS, and SCC, and for FR no-reference metrics, including  $D_\lambda$ ,  $D_s$ , and HQNR, as detailed in App. D.2.
- **Implementation details (App. E).** We give complete settings for both stages. This includes the single-band VAE conversion and latent-scale calibration, diffusion training and inference hyperparameters, and metadata-prompt construction in Table 7. We also detail test-time control and sampling choices in Figs. 7–8, together with shared preprocessing and valid-region handling.
- **Extended results and visualizations (App. F).** We report full per-sensor RR and FR results, with GF2 summarized in Table 8, and provide additional qualitative comparisons in Figs. 9–12. We further include zero-shot transfer to unseen sensors to complement the main-paper evaluation.

**A.1. Notation Summary**

Notations	Definitions
<i>Notations of Data</i>	<i>Definitions of Data</i>
$(P, M, X, S) \sim \mathcal{D}$ $P \in \mathbb{R}^{1 \times H \times W}$ $M \in \mathbb{R}^{B \times h \times w}$ $M^{(b)} \in \mathbb{R}^{1 \times h \times w}$ $\tilde{M} = \text{Up}(M)$ $\tilde{M}^{(b)} \in \mathbb{R}^{1 \times H \times W}$ $X \in \mathbb{R}^{B \times H \times W}$ $X^{(b)} \in \mathbb{R}^{1 \times H \times W}$ $B, b$ $r$ $S$	Sample: PAN $P$ , LRMS $M$ , (RR) HRMS $X$ , sensor ID $S$ . Panchromatic (PAN) image at full resolution. Low-resolution MS image with $B$ bands. The $b$ -th MS band of $M$ , $b \in \{1, \dots, B\}$ . Upsampled LRMS aligned to PAN scale (e.g., bicubic), $\tilde{M} \in \mathbb{R}^{B \times H \times W}$ . The $b$ -th MS band of $\tilde{M}$ . HRMS reference/target (available in RR; absent in FR). The $b$ -th MS band of $X$ . Number of MS bands / band index. PAN-to-MS scale ratio: $r = H/h = W/w$ . Sensor index / identity used for conditioning.
<i>Notations of Model</i>	<i>Definitions of Model</i>
$\mu_\phi(\cdot), D_\psi(\cdot)$ $\kappa_{\text{vae}}$ $f_\theta(\cdot)$ $\Phi_j^\ell(\cdot)$ $\Pi_{t \rightarrow j}^\ell, \Pi_{j \rightarrow t}^\ell$ $L(\cdot)$ $H(x) = x - L(x)$ RCBA( $\cdot$ ) $s_{S,b}$ $\text{Enc}_{\text{text}}(\cdot)$ $E(s_{S,b}) = \text{Enc}_{\text{text}}(s_{S,b})$ $W_Q, W_K, W_V$ $W_{\text{out}}, \eta$	Single-band VAE encoder mean / decoder (image $\leftrightarrow$ latent). Latent scaling factor for VAE latents. Diffusion denoiser predicting $\hat{\epsilon}$ . Narrow residual stack in branch $j \in \{\text{spa, spe}\}$ at UNet level $\ell$ . Residual adapters between trunk $t$ and branch $j$ at level $\ell$ . Fixed low-pass operator on feature residuals. Fixed high-pass operator (complement of $L$ ). Region-based cross-band attention module. Sensor-band prompt token (metadata). Frozen CLIP text encoder for prompts. Prompt embedding used for diffusion conditioning. Trainable cross-attention projections for prompt alignment. RCBA output projection and residual scale (often zero-initialized for stability).
<i>Notations of Variables</i>	<i>Definitions of Variables</i>
$z_0^{(b)} = \kappa_{\text{vae}} \mu_\phi(X^{(b)})$ $z_t^{(b)}$ $z_T$ $t \in \{1, \dots, T\}$ $T/K$ $\epsilon^{(b)} \sim \mathcal{N}(0, I)$ $\hat{\epsilon}^{(b)}$ $\beta_t$ $\bar{\alpha}_t$ $\hat{z}_0^{(b)}$ $h^\ell$ $s_j^\ell$ $\hat{s}_j^\ell$ $\Delta_j^\ell$ $L_{\text{enc}}, L_{\text{mid+dec}}$ $\lambda_{\text{spe}}, \lambda_{\text{spa}}$	Clean latent for band $b$ (VAE-encoded and scaled). Noised latent at diffusion timestep $t$ for band $b$ . Initial Gaussian latent; broadcast to all bands ( $z_T^{(b)} = z_T$ ). Diffusion timestep. Training diffusion steps / reverse steps at inference (NFE). Forward-process Gaussian noise. Predicted noise from $f_\theta$ . Noise schedule coefficient; $\alpha_t = 1 - \beta_t$ , $\bar{\alpha}_t = \prod_{i=1}^t \alpha_i$ . Cumulative noise-schedule coefficient. Predicted clean latent reconstructed from $(z_t^{(b)}, \hat{\epsilon}^{(b)})$ . Trunk feature at UNet level $\ell$ . Branch feature at level $\ell$ , $j \in \{\text{spa, spe}\}$ . Updated branch feature after coupling at level $\ell$ (Eq.(5)(6)). Projected branch residual injected into trunk at level $\ell$ . Encoder block indices / mid+decoder block indices (Eq.(5)(6)). Test-time weights for LF spectral / HF spatial injection.
<i>Notations of Learning Objective</i>	<i>Definitions of Learning Objective</i>
$\mathcal{L}_{\text{vae}}$ $\mathcal{L}_{\text{diff}}$ $\hat{X}^{(b)} = D_\psi(\hat{z}_0^{(b)} / \kappa_{\text{vae}})$	Stage-I VAE training loss. Stage-II noise MSE: $\mathbb{E}_{(P, M, X, S), b, t} \left[ \ \epsilon^{(b)} - \hat{\epsilon}^{(b)}\ _2^2 \right]$ . Band-wise decoded output; stack over $b$ to form $\hat{X} \in \mathbb{R}^{B \times H \times W}$ .

## B. Inductive Biases for Sensor-dependent PAN-MS Coupling

We follow Sec. 3: pansharpening reconstructs HRMS  $X$  from PAN  $P$  and LRMS  $M$ . Most learning-based methods are trained and evaluated under reduced-resolution RR synthesis and deployed on native full-resolution FR acquisitions where HRMS ground truth is typically unavailable. Cross-satellite studies indicate that SRF and MTF differences, together with radiometric calibration, change the effective PAN-MS coupling across sensors, and RR degradations such as Wald-type protocols may not match the native FR imaging pipeline (Wald et al., 1997; Deng et al., 2022; Ma et al., 2025). This creates systematic RR-to-FR and cross-sensor gaps when the PAN-MS relation is treated as sensor-invariant.

Up to radiometric normalization, a sensor-indexed forward model is

$$M_b = \mathcal{D}_r \left( k^{(S)} * X_b \right) + \epsilon_b, \quad P = \kappa^{(S)} * \left( \sum_{b=1}^B w_b^{(S)} X_b \right) + \epsilon_p, \quad (13)$$

where  $S$  indexes the sensor,  $w^{(S)}$  captures SRF-induced spectral mixing, and  $k^{(S)}, \kappa^{(S)}$  capture sensor-specific spatial transfer.

**Prior 1: Sensor-dependent PAN-MS mixing.** PAN integrates radiance over a sensor-specific spectral response and can be approximated as a sensor-dependent mixture of MS bands (Vivone et al., 2018). Thus, the association between  $P$  and MS channels varies with  $S$ , and cross-sensor degradation arises when a fixed mixing is implicitly assumed (Deng et al., 2022). We expose this dependence through sensor and band metadata in a fixed prompt template

$$s_{S,b} = s_S^{\text{data}} \| s_{S,b}^{\text{band}}, \quad (14)$$

which is embedded as  $\mathcal{E}(s_{S,b})$  and used to condition band-wise denoising in Eq. (3).

**Empirical evidence.** Let  $\tilde{M} = \mathcal{U}_r(M)$  denote the aligned upsampled LRMS at PAN scale, corresponding to  $\text{LMS}$  in PanCollection. For each sensor  $S$ , we fit an effective linear surrogate

$$P \approx \sum_{b=1}^B w_b^{(S)} \tilde{M}_b + c^{(S)}, \quad (15)$$

using ridge regression on randomly subsampled pixel pairs pooled within that sensor. Fig. 5 shows substantial cross-sensor variation in  $\{w_b^{(S)}\}$ , which directly supports Prior 1.

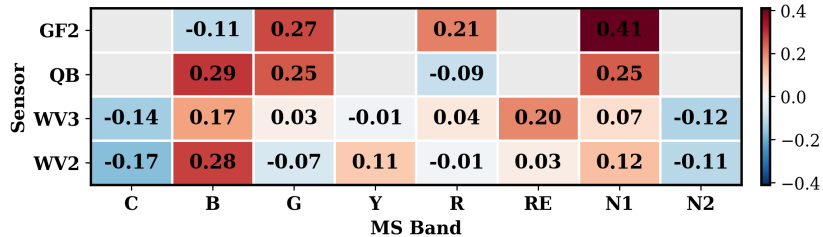


**Figure 5. Sensor-dependent PAN-MS mixing on PanCollection.** Heatmap of ridge-regression coefficients  $\{w_b^{(S)}\}$  in Eq. (15) fitted from aligned  $\tilde{M}_b$  to PAN  $P$ . Rows denote sensors and columns denote MS bands  $b \in \{C, B, G, Y, R, RE, N1, N2\}$ . Blank entries indicate bands unavailable for that sensor. Coefficients are normalized within each sensor for visualization, and the cross-row differences reveal substantial sensor dependence in the effective PAN-MS coupling.

**Connection to our formulation.** Since the coupling varies with  $S$  and the number of bands varies across sensors, we avoid hard-coding a fixed multichannel interface. We encode each band with a shared single-channel VAE in Sec. 3.3,

$$\mathbf{z}_0^{(b)} = \kappa_{\text{vae}} \boldsymbol{\mu}_\phi(\mathbf{X}^{(b)}), \quad (16)$$

and learn band-wise latent denoising conditioned on  $P, \tilde{M}^{(b)}$ , and metadata,

$$\hat{\epsilon}^{(b)} = f_\theta \left( \mathbf{z}_t^{(b)}, t; \mathbf{P}, \tilde{\mathbf{M}}^{(b)}, \mathcal{E}(s_{S,b}) \right), \quad (17)$$

which explicitly represents a sensor- and band-indexed relation rather than assuming a sensor-invariant PAN-MS mixing.

**Prior 2: Sensor-dependent spatial transfer induces RR–FR mismatch in high frequencies.** RR synthesis replaces the native spatial transfers in Eq. (13) with synthetic degradations, so the PAN–MS relation learned on RR need not match FR. The mismatch is frequency-selective and is strongest at high frequencies, which makes rigid PAN-driven detail injection brittle under RR-to-FR deployment.

**Mechanistic explanation via high-frequency alignment.** Define a fixed high-pass operator  $H(\cdot) = I - L(\cdot)$ , where  $L$  is a shared low-pass filter. For each MS band  $b$ , we measure the PAN–MS high-frequency relation by

$$\rho_{\text{HF}}^{(b)} = \text{corr}\left(H(P), H(\tilde{M}_b)\right), \quad (18)$$

computed over spatial pixels per image or crop after mean subtraction. In the Fourier domain, Eq. (13) implies

$$\widehat{H}(\tilde{M}_b)(\omega) \approx \widehat{H}(\omega) \widehat{U_r D_r}(\omega) \widehat{k^{(S)}}(\omega) \widehat{X_b}(\omega), \quad \widehat{H}(P)(\omega) \approx \widehat{H}(\omega) \widehat{\kappa^{(S)}}(\omega) \widehat{X_{\text{mix}}^{(S)}}(\omega), \quad (19)$$

so changes in  $\widehat{k^{(S)}}$  and  $\widehat{\kappa^{(S)}}$  alter relative high-frequency content and shift  $\rho_{\text{HF}}^{(b)}$ .

**Quantification on PanCollection.** We quantify the RR-to-FR shift per band by

$$\Delta\rho^{(b)} = \mathbb{E}_{\text{FR}}[\rho_{\text{HF}}^{(b)}] - \mathbb{E}_{\text{RR}}[\rho_{\text{HF}}^{(b)}], \quad (20)$$

computed with identical preprocessing and sampling for RR and FR. Fig. 6 reports empirical CDFs of  $\rho_{\text{HF}}^{(b)}$  and shows a consistent left shift from RR to FR, indicating weaker PAN–MS high-frequency alignment in native FR acquisitions and band-dependent shift magnitudes.

**Connection to our control design.** The RR-to-FR decrease in  $\rho_{\text{HF}}^{(b)}$  indicates that PAN and band-wise  $\tilde{M}_b$  are less aligned in high frequencies on FR, so a sensor-invariant HF injection learned on RR can over-trust PAN HF on FR. We therefore separate spatial and radiometric guidance in Sec. 3.4.1. A PAN-driven spatial branch and an LRMS-driven spectral branch produce residual controls  $\Delta_{\text{spa}}^{\ell}$  and  $\Delta_{\text{spe}}^{\ell}$  through lightweight adapters in Eqs. (5)–(6). These controls are fused by frequency-split injection,

$$\mathbf{h}_{\text{out}}^{\ell} = \mathbf{h}^{\ell} + \lambda_{\text{spe}} \mathcal{L}(\Delta_{\text{spe}}^{\ell}) + \lambda_{\text{spa}} \mathcal{H}(\Delta_{\text{spa}}^{\ell}), \quad \mathcal{H}(\mathbf{x}) = \mathbf{x} - \mathcal{L}(\mathbf{x}), \quad (21)$$

which anchors low-frequency radiometry to LRMS and restricts PAN guidance to high-frequency refinement, improving robustness under RR-to-FR deployment.

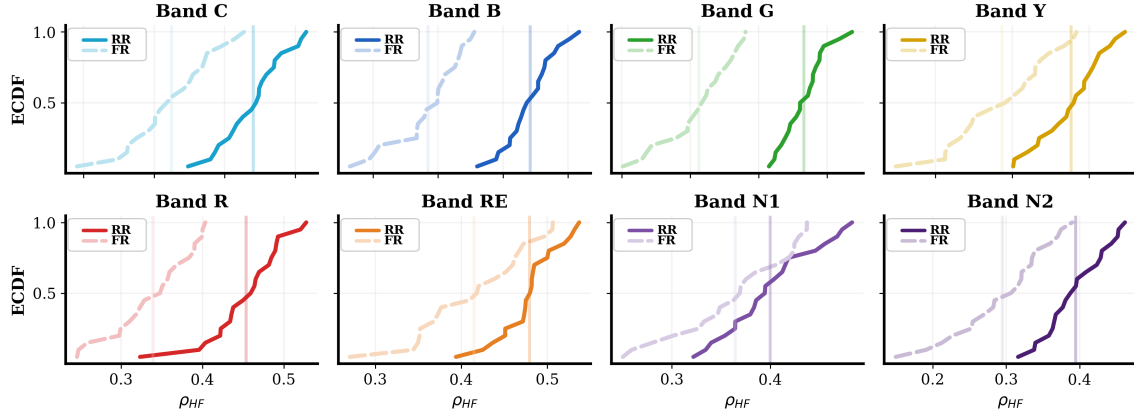


**Figure 6. WV3 RR vs. FR: PAN–MS high-frequency alignment shifts.** For each band  $b$ , we compute  $\rho_{\text{HF}}^{(b)} = \text{corr}\left(H(P), H(\tilde{M}_b)\right)$  (Eq. (18)) with the same  $H(\cdot)$  and preprocessing in RR (solid) and FR (dashed). Each subplot shows the empirical CDF over images/crops. FR consistently shifts left, indicating weaker PAN–MS high-frequency alignment, with band-dependent magnitude; vertical lines mark means.

## C. Dataset Descriptions

**Dataset overview.** We conduct experiments on the PanCollection benchmark, which provides co-registered panchromatic and multispectral image pairs from multiple satellite sensors under two standard settings (Deng et al., 2022). The reduced-resolution setting is provided as ReducedData and denoted as RR. The full-resolution setting is provided as FullData and denoted as FR. All sensors share the same spatial resolution ratio  $r = 4$  between PAN and MS. Samples are stored in .h5 files with layout  $N \times C \times H \times W$ . Each sample includes PAN  $P$  in /PAN, low-resolution MS  $M$  in /MS, and the dataset-provided upsampled and co-registered MS  $\tilde{M}$  at the PAN scale in /LMS. RR additionally provides a pseudo ground-truth high-resolution MS target  $X$  in /GT, enabling full-reference evaluation. Key names may differ in letter case across releases. We map both variants to a unified interface and use the canonical names /PAN, /MS, /LMS, and /GT throughout.

**Sensors, band configurations, and patch sizes.** PanCollection includes QuickBird, GaoFen-2, WorldView-3, and WorldView-2. QuickBird and GaoFen-2 provide 4-band MS, while WorldView-3 and WorldView-2 provide 8-band MS. Under RR, /MS has size  $64 \times 64$  and /PAN, /LMS, /GT have size  $256 \times 256$ . Under FR, /MS has size  $128 \times 128$  and /PAN and /LMS have size  $512 \times 512$ . FR does not provide /GT. Table 6 summarizes per-sensor ground sampling distance, band count, and split sizes used in this work.

**Splits, joint training, and strict zero-shot protocol.** We follow the official scene-level splits provided by PanCollection to prevent spatial leakage across training, validation, and testing. In our default setting, a single model is trained on the RR training splits of QuickBird, GaoFen-2, and WorldView-3, and validated on their RR validation splits. WorldView-2 is treated as an unseen sensor and used only for testing in both RR and FR. No WorldView-2 samples are used for training, validation, early stopping, or any model selection.

Joint training is formulated as an equal-weight multi-sensor objective

$$\min_{\theta} \frac{1}{|\mathcal{S}_{\text{train}}|} \sum_{s \in \mathcal{S}_{\text{train}}} \mathbb{E}_{(P, M, X) \sim \mathcal{D}_s} [\mathcal{L}(\theta; P, M, X, s)], \quad (22)$$

where  $\mathcal{S}_{\text{train}} = \{\text{QuickBird, GaoFen-2, WorldView-3}\}$  and  $\mathcal{D}_s$  denotes the sensor-specific RR training distribution. We implement Eq. (22) by strict round-robin scheduling at the optimizer-step level. At step  $k$ , we select the sensor

$$s_k = \mathcal{S}_{\text{train}} [k \bmod |\mathcal{S}_{\text{train}}|], \quad (23)$$

then draw a mini-batch  $\mathcal{B}_k \sim \mathcal{D}_{s_k}$  and update  $\theta$  using  $\nabla_{\theta} \mathcal{L}(\theta; \mathcal{B}_k, s_k)$ . Each step uses data from a single sensor so that the MS band count is constant within the step. The round-robin schedule yields an exact 1:1:1 contribution over QuickBird, GaoFen-2, and WorldView-3 regardless of their dataset sizes. All methods use the same dataset-provided /LMS input and the same intensity handling.

*Table 6.* PanCollection statistics and our default usage. RR uses ReducedData and provides /GT. FR uses FullData and has no /GT. RR train and validation counts are patch-based. RR and FR test sets contain 20 images per sensor. WorldView-2 is test-only.

Sensor	MS/PAN GSD	Bands	RR Train patches	RR Val patches	RR Test images	FR Test images
GaoFen-2	4.00 m / 1.00 m	4	19344	2201	20	20
QuickBird	2.40 m / 0.60 m	4	10949	1905	20	20
WorldView-3	1.24 m / 0.31 m	8	7787	1080	20	20
WorldView-2	1.84 m / 0.46 m	8	0	0	20	20

**RR evaluation protocol.** We use PanCollection ReducedData directly for RR evaluation. Each RR sample provides PAN  $P$  from /PAN, LRMS  $M$  from /MS, aligned upsampled MS  $\tilde{M}$  from /LMS, and pseudo ground-truth HRMS  $X$  from /GT. All methods take  $P$  and  $\tilde{M}$  as inputs and predict fused HRMS  $\hat{X}$  at the PAN scale. We report full-reference metrics computed between  $\hat{X}$  and  $X$ . Metric definitions and computation details are provided in Appendix D.

**FR evaluation protocol.** We use PanCollection FullData directly for FR evaluation. Each FR sample provides PAN  $P$  from /PAN, LRMS  $M$  from /MS, and aligned upsampled MS  $\tilde{M}$  from /LMS. All methods take  $P$  and  $\tilde{M}$  as inputs and predict  $\hat{X}$ . Since FR does not include ground-truth HRMS, we report no-reference QNR-based measures and qualitative comparisons. Metric definitions and computation details are provided in Appendix D.

## D. Evaluation

### D.1. Compared Methods

**SGDiff** (Xing et al., 2025) proposes a semantic-guided diffusion model for general pansharpening across different sensors and scenes. It models the HRMS residual over the upsampled LRMS with a 3D Transformer denoiser. A pretrained geoscience VLM (GeoChat) provides global semantics and grounded regional descriptions, which are encoded into routing scores to sparsely activate and re-weight experts in a semantic-guided MoE module.

**SSDiff** (Zhong et al., 2024) formulates pansharpening from a subspace decomposition viewpoint, separating spatial details and spectral components within a two-branch diffusion framework. It couples the two branches via alternating projection and exchanges high-frequency cues through Fourier-based modulation during denoising. A branch-wise alternating fine-tuning strategy (LoRA-like) is further used to enhance component-specific representations.

**PanDiff** (Meng et al., 2023) introduces a DDPM-based framework that learns the distribution of the difference map between HRMS and interpolated MS. It performs multi-step conditional denoising with a U-Net backbone, injecting PAN and LRMS as guidance at each step. A modal intercalibration module aligns spatial and spectral cues to strengthen the conditioning.

**WFANet** (Huang et al., 2025b) is a wavelet-assisted multi-frequency attention network. It decomposes PAN features into frequency bands with discrete wavelet transforms, and fuses LRMS spectra with frequency-specific spatial cues using a multi-frequency fusion attention module, followed by inverse-wavelet reconstruction. A wavelet pyramid and a spatial detail enhancement module further improve multi-scale fusion and high-frequency recovery.

**ARConv** (Wang et al., 2025) introduces an adaptive rectangular convolution that predicts kernel height and width from features and adjusts sampling accordingly. It builds a lightweight rectangular deformable sampling map and applies an affine transformation to improve spatial adaptability. Based on ARConv, ARNet replaces standard convolutions in a U-Net-style backbone to better handle scale-varying structures.

**BiMPan** (Hou et al., 2023) proposes bidomain modeling that combines band-adaptive local modeling in the spatial domain with global detail reconstruction in the Fourier domain. It uses band-specific adaptive convolutions for local spectral structures and a Fourier global modeling module for global spatial details, and fuses the two to generate HRMS outputs.

**LAGConv** (Jin et al., 2022) proposes a content-adaptive convolution that combines locally adaptive kernel weighting with a global harmonic bias. It predicts pixel-wise scaling factors over a shared base kernel and injects a global bias derived from pooled features to improve coherence. Plugging LAGConv into a lightweight residual fusion network yields improved adaptation to spatially varying patterns.

**FusionNet** (Deng et al., 2020) is a detail-injection CNN that predicts spatial details from the band-wise difference between replicated PAN and upsampled LRMS using a ResNet-style backbone. The predicted residual is added to the upsampled LRMS to obtain the fused HRMS image.

**PanNet** (Yang et al., 2017) trains in the high-pass domain to emphasize spatial detail learning. It feeds high-frequency PAN and upsampled LRMS into a ResNet to predict detail residuals, which are injected through a spectra-mapping skip connection to produce the final HRMS output and improve cross-satellite generalization.

### D.2. Metrics

**Notation.** Let  $\mathbf{F} \in \mathbb{R}^{B \times H \times W}$  be the fused HRMS and  $\mathbf{P} \in \mathbb{R}^{1 \times H \times W}$  the PAN image. Under the reduced-resolution protocol,  $\mathbf{R} \in \mathbb{R}^{B \times H \times W}$  denotes the HRMS reference. Let  $\mathbf{M} \in \mathbb{R}^{B \times h \times w}$  be the LRMS image and  $r = H/h = W/w$  the resolution ratio. All metrics are computed on a valid pixel set  $\Omega$  defined by the same border handling used in our experiments.

**Local operator (UIQI).** For single-band  $\mathbf{X}, \mathbf{Y}$  at the same resolution, we compute window-averaged UIQI. On a window  $\mathcal{W} \subset \Omega$ ,

$$q(\mathbf{X}, \mathbf{Y}; \mathcal{W}) = \frac{2\mu_X\mu_Y}{\mu_X^2 + \mu_Y^2 + \epsilon} \cdot \frac{2\sigma_{XY}}{\sigma_X^2 + \sigma_Y^2 + \epsilon}, \quad (24)$$

and  $Q(\mathbf{X}, \mathbf{Y})$  is the average of  $q(\cdot, \cdot; \mathcal{W})$  over all sliding windows. We use window size  $w = 32$ , stride  $s = 1$ , and  $\epsilon = 10^{-12}$ .

**Reduced-Resolution metrics (RR).** With reference  $\mathbf{R}$  available, RR metrics explicitly measure *spectral fidelity* (color preservation) and *spatial fidelity* (detail injection) of  $\mathbf{F}$ .

**Q4/Q8** are multiband extensions of UIQI and evaluate *joint spectral-spatial similarity* between  $\mathbf{F}$  and  $\mathbf{R}$  by correlating local statistics across bands. We compute them locally with the same window setting as  $Q(\cdot, \cdot)$  and average over windows and images (higher is better).

**SAM** emphasizes *spectral (chromatic) distortion* by comparing the angle between spectral vectors:

$$\text{SAM} = \frac{180}{\pi} \cdot \frac{1}{|\Omega_{\text{sam}}|} \sum_{p \in \Omega_{\text{sam}}} \arccos \left( \text{clip} \left( \frac{\langle \mathbf{f}_p, \mathbf{r}_p \rangle}{\|\mathbf{f}_p\|_2 \|\mathbf{r}_p\|_2}, -1, 1 \right) \right), \quad \Omega_{\text{sam}} = \{p \in \Omega : \|\mathbf{f}_p\|_2 > \epsilon \wedge \|\mathbf{r}_p\|_2 > \epsilon\}. \quad (25)$$

Lower is better.

**ERGAS** focuses on *global radiometric distortion* by aggregating band-wise relative RMSE (scale-normalized by the reference mean):

$$\text{ERGAS} = 100 \cdot r \sqrt{\frac{1}{B} \sum_{b=1}^B \left( \frac{\text{RMSE}_b}{\mu_b + \epsilon} \right)^2}, \quad \text{RMSE}_b = \sqrt{\frac{1}{|\Omega|} \sum_{p \in \Omega} (\mathbf{F}_{b,p} - \mathbf{R}_{b,p})^2}, \quad \mu_b = \frac{1}{|\Omega|} \sum_{p \in \Omega} \mathbf{R}_{b,p}. \quad (26)$$

Lower is better.

**SCC** targets *spatial detail transfer* by correlating high-frequency structures (Sobel gradients) between  $\mathbf{P}$  and each fused band:

$$\text{SCC} = \frac{1}{B} \sum_{b=1}^B \rho(\nabla(\mathbf{P}), \nabla(\mathbf{F}_b)), \quad \rho(\mathbf{x}, \mathbf{y}) = \frac{\sum_{p \in \Omega} (x_p - \bar{x})(y_p - \bar{y})}{\sqrt{\sum_{p \in \Omega} (x_p - \bar{x})^2 + \epsilon} \sqrt{\sum_{p \in \Omega} (y_p - \bar{y})^2 + \epsilon}}. \quad (27)$$

If  $\rho$  is undefined due to (near-)zero variance, we set it to 0. Higher is better.

**Full-Resolution metrics (FR).** Without reference HRMS, FR metrics assess distortions by enforcing *cross-scale consistency*: spectral relationships should match the LRMS, and spatial relationships should match the PAN.

**Scale alignment.** Let  $\text{Up}_r(\cdot)$  and  $\text{Down}_r(\cdot)$  denote bicubic up/downsampling by factor  $r$ . We set  $\hat{\mathbf{M}} = \text{Up}_r(\mathbf{M})$  (PAN scale) and  $\hat{\mathbf{F}}_i = \mathbf{F}_i$ .

**PAN degradation.** We construct an MS-scale PAN proxy by Gaussian low-pass filtering followed by downsampling:

$$\mathbf{P}_\downarrow = \text{Down}_r(G_\sigma * \mathbf{P}), \quad \sigma = \frac{r}{2}, \quad k = 9, \quad \hat{\mathbf{P}}_\downarrow = \text{Up}_r(\mathbf{P}_\downarrow), \quad (28)$$

so that all  $Q(\cdot, \cdot)$  evaluations below are performed at PAN scale.

$D_\lambda$  measures *spectral distortion* by comparing inter-band dependency (local UIQI) between the fused image and the upsampled LRMS:

$$D_\lambda = \frac{1}{B(B-1)} \sum_{i \neq j} \left| Q(\hat{\mathbf{F}}_i, \hat{\mathbf{F}}_j) - Q(\hat{\mathbf{M}}_i, \hat{\mathbf{M}}_j) \right|. \quad (29)$$

Lower is better.

$D_s$  measures *spatial distortion* by comparing PAN consistency of fused bands against that of the LRMS, using a scale-degraded PAN proxy:

$$D_s = \frac{1}{B} \sum_{i=1}^B \left| Q(\hat{\mathbf{F}}_i, \mathbf{P}) - Q(\hat{\mathbf{M}}_i, \hat{\mathbf{P}}_\downarrow) \right|. \quad (30)$$

Lower is better.

**HQNR** aggregates spectral and spatial distortions:

$$\text{HQNR} = (1 - D_\lambda)(1 - D_s), \quad (31)$$

where higher is better.

## E. Implementation Details

### E.1. Stage I: Single-band VAE

Stage I adapts the Stable Diffusion v1.5 VAE to remote-sensing HRMS patches and converts it into a *single-band* encoder-decoder shared across all spectral bands. We only modify the first and last convolutional layers that interface with image channels, while keeping all intermediate layers unchanged. Given a multispectral patch  $X \in \mathbb{R}^{B \times H \times W}$ , we fold the spectral dimension into the batch dimension so that each band  $X^{(b)} \in \mathbb{R}^{1 \times H \times W}$  becomes one sample and is processed by the same single-band VAE.

**Training objective.** For a single-band input  $x = X^{(b)} \in \mathbb{R}^{1 \times H \times W}$ , the encoder defines  $q_\phi(z \mid x) = \mathcal{N}(\mu_\phi(x), \text{diag}(\sigma_\phi^2(x)))$  and the decoder reconstructs  $\hat{x} = D_\psi(z)$  with  $z \sim q_\phi(z \mid x)$ . Stage I minimizes a weighted reconstruction-regularization objective:

$$\mathcal{L}_{\text{vae}} = \lambda_{\text{rec}} \mathbb{E}_{z \sim q_\phi(z \mid x)} [\ell_{\text{rec}}(x, D_\psi(z))] + \lambda_{\text{kl}} \text{KL}(q_\phi(z \mid x) \parallel \mathcal{N}(0, I)), \quad (32)$$

where  $\ell_{\text{rec}}$  is a pixel-space reconstruction criterion. We average Eq. (32) over bands and training patches by folding the band dimension into the batch dimension.

**Single-band conversion and weight initialization.** Let the original SD-VAE encoder input convolution be

$$\text{Conv}_{\text{in}}(x) = W_{\text{in}} * x + b_{\text{in}}, \quad W_{\text{in}} \in \mathbb{R}^{C \times 3 \times k \times k}, \quad b_{\text{in}} \in \mathbb{R}^C, \quad (33)$$

and the converted single-band convolution be

$$\text{Conv}'_{\text{in}}(g) = W'_{\text{in}} * g + b'_{\text{in}}, \quad W'_{\text{in}} \in \mathbb{R}^{C \times 1 \times k \times k}. \quad (34)$$

We initialize  $W'_{\text{in}}$  by enforcing *functional equivalence* on a pseudo-RGB embedding. For a single-band input  $g$ , define

$$T(g) = \begin{bmatrix} \alpha_R g \\ \alpha_G g \\ \alpha_B g \end{bmatrix}, \quad \alpha_R + \alpha_G + \alpha_B = 1. \quad (35)$$

Requiring  $\text{Conv}'_{\text{in}}(g) = \text{Conv}_{\text{in}}(T(g))$  at initialization and using channel-wise linearity of convolution,

$$\text{Conv}_{\text{in}}(T(g)) = \sum_{c \in \{R, G, B\}} W_{\text{in}}^{(c)} * (\alpha_c g) + b_{\text{in}} = \left( \sum_c \alpha_c W_{\text{in}}^{(c)} \right) * g + b_{\text{in}}, \quad (36)$$

we obtain the exact warm start

$$W'_{\text{in}} = \sum_{c \in \{R, G, B\}} \alpha_c W_{\text{in}}^{(c)}, \quad b'_{\text{in}} = b_{\text{in}}. \quad (37)$$

We use the standard luminance coefficients  $(\alpha_R, \alpha_G, \alpha_B) = (0.299, 0.587, 0.114)$ . Besides matching natural-image intensity statistics, the constraint  $\sum_c \alpha_c = 1$  preserves DC response: if  $x_R = x_G = x_B = g$  then  $\alpha^\top x = g$ .

For the decoder, let

$$y = \text{Conv}_{\text{out}}(h) = W_{\text{out}}^{\text{vae}} * h + b_{\text{out}}^{\text{vae}}, \quad W_{\text{out}}^{\text{vae}} \in \mathbb{R}^{3 \times C \times k \times k}, \quad b_{\text{out}}^{\text{vae}} \in \mathbb{R}^3. \quad (38)$$

We define the single-band output as the luminance projection  $\hat{g} = \sum_c \alpha_c y_c$ . By linearity,

$$W'_{\text{out}} = \sum_{c \in \{R, G, B\}} \alpha_c (W_{\text{out}}^{\text{vae}})^{(c)}, \quad b'_{\text{out}} = \sum_{c \in \{R, G, B\}} \alpha_c (b_{\text{out}}^{\text{vae}})^{(c)}. \quad (39)$$

Eqs. (37)–(39) ensure that, at initialization, the converted VAE behaves identically to the original SD-VAE applied to the embedding  $T(g)$ , reducing distribution drift after channel conversion.

After Stage I converges, we calibrate a *global* latent scaling factor  $\kappa$  and keep it fixed throughout Stage II training and inference.

**Latent scaling factor  $\kappa$ .** Stage II performs diffusion in the VAE latent space under the convention that the clean latent has near-unit scale. After single-band conversion and fine-tuning, the latent magnitude may drift, so we re-estimate a global scale  $\kappa$  after Stage I:

$$z_0^{(b)} = \kappa E(X^{(b)}), \quad \hat{X}^{(b)} = D(\hat{z}_0^{(b)} / \kappa), \quad (40)$$

where  $E(\cdot)$  and  $D(\cdot)$  are the VAE encoder and decoder.

**Which latent is calibrated.** Let  $q_\phi(z | x) = \mathcal{N}(\mu_\phi(x), \text{diag}(\sigma_\phi^2(x)))$ . Since Stage II uses the posterior mean as the clean latent, we set  $E(x) = \mu_\phi(x)$  and calibrate  $\kappa$  using

$$u := \mu_\phi(x) \in \mathbb{R}^d, \quad (41)$$

where  $d$  is the flattened latent dimensionality.

**Derivation via KL-optimal isotropic calibration.** Approximating  $u$  by a Gaussian with mean  $m = \mathbb{E}[u]$  and covariance  $\Sigma = \mathbb{E}[(u - m)(u - m)^\top]$ , scaling  $z = \kappa u$  yields  $z \sim \mathcal{N}(\kappa m, \kappa^2 \Sigma)$ . We choose  $\kappa > 0$  to best match the unit-Gaussian convention:

$$\kappa^* = \arg \min_{\kappa > 0} \text{KL}(\mathcal{N}(\kappa m, \kappa^2 \Sigma) \| \mathcal{N}(0, I)). \quad (42)$$

Using the Gaussian KL,

$$\begin{aligned} \text{KL} &= \frac{1}{2} \left( \text{tr}(\kappa^2 \Sigma) + \|\kappa m\|_2^2 - d - \log \det(\kappa^2 \Sigma) \right) \\ &= \frac{1}{2} \left( \kappa^2 (\text{tr} \Sigma + \|m\|_2^2) - d - d \log \kappa^2 \right) + \text{const}, \end{aligned} \quad (43)$$

so  $\partial \text{KL} / \partial \kappa = 0$  gives

$$\kappa^{*2} = \frac{d}{\text{tr} \Sigma + \|m\|_2^2} = \frac{d}{\mathbb{E} \|u\|_2^2} \implies \kappa^* = \sqrt{\frac{d}{\mathbb{E} \|u\|_2^2}} = \frac{1}{\sqrt{\mathbb{E} \left[ \frac{1}{d} \|u\|_2^2 \right]}}. \quad (44)$$

Thus,  $\kappa^*$  makes the average latent energy  $\mathbb{E}[\|z\|_2^2 / d]$  close to 1.

**Why scale matters for diffusion.** For DDPM-style forward diffusion  $x_t = \sqrt{\bar{\alpha}_t} x_0 + \sqrt{1 - \bar{\alpha}_t} \epsilon$  with  $\epsilon \sim \mathcal{N}(0, I)$ , a variance shift  $\text{Var}(x_0) \mapsto c^2 \text{Var}(x_0)$  changes the effective signal-to-noise ratio

$$\text{SNR}_t = \frac{\bar{\alpha}_t \text{Var}(x_0)}{1 - \bar{\alpha}_t} \mapsto \frac{\bar{\alpha}_t c^2 \text{Var}(x_0)}{1 - \bar{\alpha}_t}, \quad (45)$$

misaligning the designed noise schedule. Eq. (44) enforces  $\text{Var}(x_0) \approx 1$  (in the per-dimension energy sense), restoring schedule compatibility.

**Estimator.** We approximate the expectation in Eq. (44) with  $N = 10,000$  randomly sampled training patches. For  $u_i = \mu_\phi(x_i) \in \mathbb{R}^d$ ,

$$\hat{s}^2 = \frac{1}{N} \sum_{i=1}^N \left( \frac{1}{d} \|u_i\|_2^2 \right), \quad \kappa = \frac{1}{\sqrt{\hat{s}^2 + \epsilon}}, \quad (46)$$

where  $\epsilon$  is a small constant for stability. We accumulate  $\hat{s}^2$  and then fix  $\kappa$  for all Stage II training and inference.

## E.2. Stage II: Latent Conditional Diffusion

**Training objective.** Stage II trains the denoiser by noise prediction in the VAE latent space. For each training tuple  $(P, M, X, S) \sim \mathcal{D}$  and band index  $b$ , we form the clean latent  $z_0^{(b)} = \kappa_{\text{vae}} E(X^{(b)})$  and sample a timestep  $t \sim \text{Unif}\{1, \dots, T\}$  with noise  $\epsilon^{(b)} \sim \mathcal{N}(0, I)$ :

$$z_t^{(b)} = \sqrt{\bar{\alpha}_t} z_0^{(b)} + \sqrt{1 - \bar{\alpha}_t} \epsilon^{(b)}. \quad (47)$$

The denoiser predicts  $\hat{\epsilon}^{(b)} = f_\theta(z_t^{(b)}, t; P, \tilde{M}^{(b)}, E(s_{S,b}))$  and is trained with

$$\mathcal{L}_{\text{diff}} = \mathbb{E}_{(P, M, X, S)} \mathbb{E}_{b, t, \epsilon^{(b)}} \left[ \|\epsilon^{(b)} - \hat{\epsilon}^{(b)}\|_2^2 \right]. \quad (48)$$

In Stage II, we keep the VAE and the main SD-UNet trunk frozen and optimize only the lightweight conditional modules that generate and inject residual controls.

**Dual conditional branches.** We implement spatial and spectral conditioning with two lightweight control branches attached to a largely frozen SD-UNet trunk. Each branch follows the trunk multi-resolution layout and block indexing, but uses reduced channels and learns only residual controls. We use a constant width ratio  $\rho = \frac{1}{4}$  across all levels. Let  $c^\ell$  be the trunk channel width at UNet level  $\ell$ . The branch width is  $c_j^\ell = \rho c^\ell$  for  $j \in \{\text{spa, spe}\}$ , with integer rounding when needed.

Let  $h^\ell$  denote the trunk feature at level  $\ell$ . For branch  $j \in \{\text{spa, spe}\}$ , we compute a branch feature  $s_j^\ell$  and inject a residual control  $\Delta_j^\ell$  back into the trunk. We adopt a hybrid coupling rule:

$$s_j^\ell = \begin{cases} \Phi_j^\ell(\Pi_{t \rightarrow j}^\ell(h^\ell), C_j), & \ell \in L_{\text{enc}}, \\ \Phi_j^\ell(s_j^{\ell-1}, C_j), & \ell \in L_{\text{mid+dec}}, \end{cases} \quad \Delta_j^\ell = \Pi_{j \rightarrow t}^\ell(s_j^\ell), \quad (49)$$

where  $C_{\text{spa}} = P$  and  $C_{\text{spe}} = \tilde{M}^{(b)}$ . In encoder blocks, the trunk feature  $h^\ell$  is mapped to the branch space via  $\Pi_{t \rightarrow j}^\ell$  to improve alignment. In mid and decoder blocks, trunk-to-branch feedback is removed and the branches propagate only through  $s_j^{\ell-1}$ . At all levels, the branch-to-trunk adapter  $\Pi_{j \rightarrow t}^\ell$  produces the control residual  $\Delta_j^\ell$ .

**Test-time control via  $(\lambda_{\text{spe}}, \lambda_{\text{spa}})$ .** We inject the spectral/spatial branch residuals into the trunk through a fixed frequency split:

$$h_1^\ell = h^\ell + \lambda_{\text{spe}} L(\Delta_{\text{spe}}^\ell), \quad h_{\text{out}}^\ell = h_1^\ell + \lambda_{\text{spa}} H(\Delta_{\text{spa}}^\ell), \quad (50)$$

where  $L$  is a fixed low-pass operator and  $H(\cdot) = I - L(\cdot)$  is the complementary high-pass operator. We train with  $\lambda_{\text{spe}} = \lambda_{\text{spa}} = 1$  and tune them only at inference.

*Band-selective scaling.* Let  $\widehat{L}(\omega)$  denote the Fourier response of  $L$ . Using  $H = I - L$ , the injected feature in the frequency domain becomes

$$\widehat{h_{\text{out}}^\ell}(\omega) = \widehat{h^\ell}(\omega) + \lambda_{\text{spe}} \widehat{L}(\omega) \widehat{\Delta_{\text{spe}}^\ell}(\omega) + \lambda_{\text{spa}} (1 - \widehat{L}(\omega)) \widehat{\Delta_{\text{spa}}^\ell}(\omega),$$

indicating that  $\lambda_{\text{spe}}$  controls the gain of the low-frequency components, whereas  $\lambda_{\text{spa}}$  controls the gain of the high-frequency components. Moreover, if the split is approximately energy-orthogonal, i.e.,  $\langle L(x), H(y) \rangle \approx 0$ , then

$$\begin{aligned} \|\lambda_{\text{spe}} L(\Delta_{\text{spe}}) + \lambda_{\text{spa}} H(\Delta_{\text{spa}})\|_2^2 &= \lambda_{\text{spe}}^2 \|L(\Delta_{\text{spe}})\|_2^2 + \lambda_{\text{spa}}^2 \|H(\Delta_{\text{spa}})\|_2^2 + 2\lambda_{\text{spe}}\lambda_{\text{spa}} \langle L(\Delta_{\text{spe}}), H(\Delta_{\text{spa}}) \rangle \\ &\approx \lambda_{\text{spe}}^2 \|L(\Delta_{\text{spe}})\|_2^2 + \lambda_{\text{spa}}^2 \|H(\Delta_{\text{spa}})\|_2^2, \end{aligned}$$

which explains the stable two-knob trade-off under a fixed inference pipeline.

We sweep

$$\mathcal{G} = \left\{ \lambda \mid \lambda \in \{0.5, 0.6, \dots, 1.5\} \right\}, \quad (51)$$

with a step size of 0.1, while keeping model weights, preprocessing, frequency split, sampler, noise schedule, the number of sampling steps, and random seed fixed. For a given test sample, we select the best setting by

$$(\lambda_{\text{spe}}^*, \lambda_{\text{spa}}^*) = \arg \max_{\lambda_{\text{spe}}, \lambda_{\text{spa}} \in \mathcal{G}} \text{HQNR}(\lambda_{\text{spe}}, \lambda_{\text{spa}}). \quad (52)$$

For the sample shown in Fig. 7, the optimum is  $(\lambda_{\text{spe}}^*, \lambda_{\text{spa}}^*) = (1.0, 0.9)$ .

**Inference Step Budget.** Given PAN  $P \in \mathbb{R}^{1 \times H \times W}$  and LRMS  $M \in \mathbb{R}^{B \times h \times w}$  with scale ratio  $r = H/h = W/w$ , we first align LRMS to the PAN scale via bicubic upsampling:

$$\tilde{M} = \text{Up}(M) \in \mathbb{R}^{B \times H \times W}. \quad (53)$$

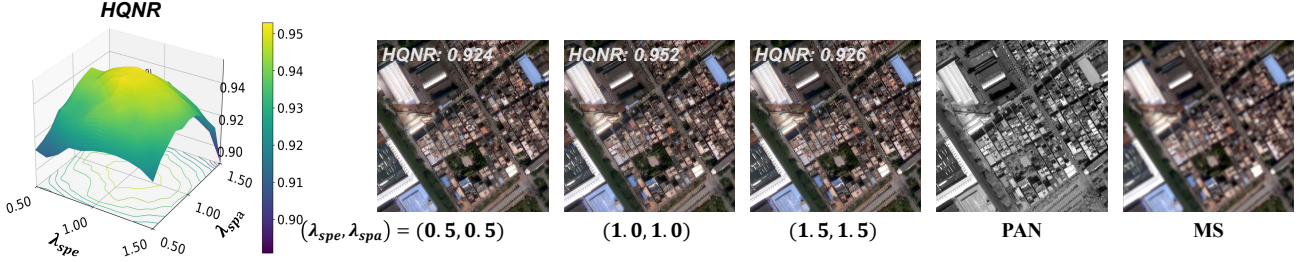


Figure 7. Test-time control by  $(\lambda_{\text{spe}}, \lambda_{\text{spa}})$ . **Left:** HQNR response surface over  $\lambda_{\text{spe}}, \lambda_{\text{spa}} \in \{0.5, 0.6, \dots, 1.5\}$  (step 0.1), where each grid point is evaluated under an identical inference pipeline. **Right:** Pan-sharpened outputs on the same test sample for three representative settings  $(0.5, 0.5)$ ,  $(1.0, 1.0)$ , and  $(1.5, 1.5)$ , with their corresponding HQNR scores; the PAN and LRMS inputs are shown for reference.

We then perform *band-wise* latent conditional diffusion. For each band  $b$ , we sample  $z_T^{(b)} \sim \mathcal{N}(0, I)$  and run a UniPC reverse process under the SD1.5 discrete noise schedule:

$$z_{t_{k-1}}^{(b)} = \text{UniPC}\left(z_{t_k}^{(b)}, \hat{\epsilon}_\theta(z_{t_k}^{(b)}, t_k; P, \tilde{M}^{(b)}), t_k \rightarrow t_{k-1}\right), \quad k = K, \dots, 1, \quad (54)$$

where each reverse update uses one denoiser forward pass, hence  $\text{NFE} = K$ .

**Shared initial noise for cross-band consistency.** Because inference is stochastic, independently sampling  $\{z_T^{(b)}\}_{b=1}^B$  can introduce band-wise sampling drift. We therefore draw a single latent per image and broadcast it across bands:

$$z_T \sim \mathcal{N}(0, I), \quad z_T^{(b)} = z_T, \quad \forall b, \quad (55)$$

which removes initial cross-band discrepancy (e.g.,  $\mathbb{E}\|z_T^{(b)} - z_T^{(b')}\|_2^2 = 0$  versus  $2d$  if independent for  $d$ -dimensional latents). For a fair step-budget comparison, we fix the random seed (thus the same  $z_T$ ) across different  $K$ .

**Budget selection.** Fig. 8 shows the quality–speed trade-off under an identical inference pipeline. As NFE increases, quality improves quickly at small budgets and becomes near-saturated around  $\text{NFE} \approx 20$  for our method (lower SAM and higher HQNR), while wall-clock latency scales approximately linearly with NFE:

$$\text{Latency}(K) \approx \tau_0 + \tau \cdot \text{NFE} = \tau_0 + \tau \cdot K. \quad (56)$$

Therefore, we adopt the smallest budget in the saturation regime (default  $K = 20$ ) to balance reconstruction quality and runtime.

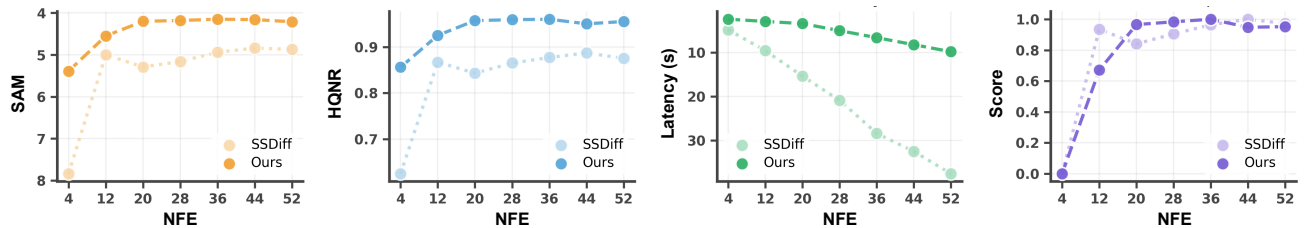


Figure 8. Effect of the reverse-step budget. We vary the number of reverse updates  $K$  under a fixed inference configuration. From left to right: RR quality (SAM↓), FR quality (HQNR↑), wall-clock latency per reconstructed image and an overall score. Our method reaches near-saturated quality at  $\text{NFE} \approx 20$  with substantially lower latency than the pixel-space diffusion baseline (SSDiff).

**Prompt Templates.** We condition the denoiser on sensor-specific and band-specific metadata via text prompts encoded by a frozen CLIP text encoder. For each sensor  $S$  and multispectral (MS) band  $b$ , we construct the prompt by concatenating two components:

$$s_{S,b} = s_S^{\text{data}} \parallel s_{S,b}^{\text{band}}, \quad (57)$$

where  $\parallel$  denotes string concatenation with a single whitespace separator. The first component  $s_S^{\text{data}}$  describes the sensor configuration, while the second component  $s_{S,b}^{\text{band}}$  specifies the attributes of band  $b$ . The band ordering follows the channel order in the dataset.

**Unified prompt templates.** We use two unified templates that work across all sensors. Angle brackets denote placeholders to be instantiated with sensor- and band-specific parameters:

$$s_S^{\text{data}} = \text{Sensor } \langle S \rangle. \text{ PAN GSD } \langle g_{\text{pan}} \rangle \text{ m. MS GSD } \langle g_{\text{ms}} \rangle \text{ m. MS bands } \langle B \rangle., \quad (58)$$

$$s_{S,b}^{\text{band}} = \text{Band } \langle \nu \rangle. \text{ Wavelength } [\langle \lambda_{\text{lo}} \rangle, \langle \lambda_{\text{hi}} \rangle] \text{ nm..} \quad (59)$$

Here,  $g_S^{\text{pan}}$  and  $g_S^{\text{ms}}$  denote the ground sampling distances (GSDs) for PAN and MS bands, respectively;  $B_S$  is the total number of MS bands;  $\nu_{S,b}$  is the human-readable band name (e.g., Blue, NIR1); and the wavelength range is specified by the lower and upper bounds  $\lambda_{S,b}^{\text{lo}}$  and  $\lambda_{S,b}^{\text{hi}}$  in nanometers.

The text encoder produces an embedding  $E(s_{S,b})$ , which is injected into the diffusion U-Net via cross-attention layers. We use the same templates for both training and inference to ensure consistency.

Sensor $S$	$g_S^{\text{pan}}$ (m)	$g_S^{\text{ms}}$ (m)	$B_S$	MS bands $\nu_{S,b}$ and wavelength range $[\lambda_{S,b}^{\text{lo}}, \lambda_{S,b}^{\text{hi}}]$ (nm)
GF2	1.00	4.00	4	Blue [450,520]; Green [520,590]; Red [630,690]; NIR [770,890]
QB	0.60	2.40	4	Blue [450,520]; Green [520,600]; Red [630,690]; NIR [760,900]
WV3	0.31	1.24	8	Coastal [400,450]; Blue [450,510]; Green [510,580]; Yellow [585,625]; Red [630,690]; RedEdge [705,745]; NIR1 [770,895]; NIR2 [860,1040]
WV2*	0.46	1.84	8	Coastal [400,450]; Blue [450,510]; Green [510,580]; Yellow [585,625]; Red [630,690]; RedEdge [705,745]; NIR1 [770,895]; NIR2 [860,1040]

Table 7. Sensor-specific parameters for prompt instantiation. \*WV2 is used only for zero-shot evaluation.

**Example instantiation.** For sensor WV3 and its fourth MS band (Yellow), the instantiated components are:

$$s_{\text{WV3}}^{\text{data}} = \text{Sensor WV3. PAN GSD } 0.31 \text{ m. MS GSD } 1.24 \text{ m. MS bands } 8.$$

$$s_{\text{WV3},4}^{\text{band}} = \text{Band Yellow. Wavelength } [585, 625] \text{ nm.}$$

$$s_{\text{WV3},4} = s_{\text{WV3}}^{\text{data}} \parallel s_{\text{WV3},4}^{\text{band}}.$$

The complete prompt for this band is the concatenation of the two components shown above.

## F. More quantitative and visualization results

This appendix complements the main paper with additional quantitative comparisons and visual examples that are not included due to page limits. Unless otherwise stated, we follow Appendix C and evaluate in two settings. We report full-reference metrics under the reduced-resolution Wald protocol and QNR-based no-reference metrics on native full-resolution acquisitions. All results are reported as mean  $\pm$  standard deviation over the official test set.

For RR, higher values indicate better performance for  $Q_4/Q_8$  and SCC, while lower values are preferred for SAM and ERGAS. For FR, lower values indicate less distortion for  $D_\lambda$  and  $D_s$ , and higher values indicate better quality for HQNR. We highlight the best and second-best results in **bold** and underlined, respectively.

### F.1. GaoFen-2 results

**Quantitative comparison.** Table 8 summarizes the complete results on GaoFen-2, abbreviated as GF2, which contains four multispectral bands. SALAD-Pan achieves the best spectral fidelity in RR, attaining the lowest SAM and ERGAS. It also delivers the most favorable FR quality, with the highest HQNR and the lowest  $D_s$ . These numbers indicate that SALAD-Pan injects spatial details in a way that is compatible with the PAN observation, while avoiding structural inconsistencies that typically arise when sharpening dominates the multispectral content. Meanwhile, the method remains competitive on overall consistency measures such as  $Q_4$  and SCC, suggesting that the gains do not come from trading off global coherence for local sharpness.

Table 8. Quantitative results on the GaoFen-2 (GF2) dataset. Best and second-best results are in **bold** and underlined.

METHODS		REDUCED RESOLUTION (RR)				FULL RESOLUTION (FR)		
MODELS	PUB/YEAR	$Q_4 \uparrow$	$SAM \downarrow$	$ERGAS \downarrow$	$SCC \uparrow$	$D_\lambda \downarrow$	$D_s \downarrow$	$HQNR \uparrow$
PANNET	ICCV'17	0.967 $\pm$ 0.013	0.997 $\pm$ 0.022	0.919 $\pm$ 0.039	0.973 $\pm$ 0.011	0.017 $\pm$ 0.012	0.047 $\pm$ 0.012	0.937 $\pm$ 0.023
FUSIONNET	TGRS'20	0.964 $\pm$ 0.014	0.974 $\pm$ 0.035	0.988 $\pm$ 0.072	0.971 $\pm$ 0.012	0.040 $\pm$ 0.013	0.101 $\pm$ 0.014	0.863 $\pm$ 0.018
LAGCONV	AAAI'22	0.970 $\pm$ 0.011	1.080 $\pm$ 0.023	0.910 $\pm$ 0.045	0.977 $\pm$ 0.006	0.033 $\pm$ 0.013	0.079 $\pm$ 0.013	0.891 $\pm$ 0.021
BiMPAN	ACMM'23	0.965 $\pm$ 0.020	0.902 $\pm$ 0.066	0.881 $\pm$ 0.058	0.972 $\pm$ 0.018	0.032 $\pm$ 0.015	0.051 $\pm$ 0.014	0.918 $\pm$ 0.019
ARCONV	CVPR'25	0.982 $\pm$ 0.013	0.710 $\pm$ 0.149	0.645 $\pm$ 0.127	<u>0.994<math>\pm</math>0.005</u>	0.007 $\pm$ 0.005	0.029 $\pm$ 0.019	0.963 $\pm$ 0.018
WFANET	AAAI'25	0.981 $\pm$ 0.007	0.751 $\pm$ 0.082	0.657 $\pm$ 0.074	<b>0.994<math>\pm</math>0.002</b>	<b>0.003<math>\pm</math>0.003</b>	0.032 $\pm$ 0.021	0.964 $\pm$ 0.020
PANDIFF	TGRS'23	0.979 $\pm$ 0.011	0.888 $\pm$ 0.037	0.746 $\pm$ 0.031	0.988 $\pm$ 0.003	0.027 $\pm$ 0.011	0.073 $\pm$ 0.013	0.903 $\pm$ 0.025
SSDIFF	NEURIPS'24	<b>0.983<math>\pm</math>0.007</b>	<u>0.670<math>\pm</math>0.124</u>	<u>0.604<math>\pm</math>0.108</u>	0.991 $\pm$ 0.006	0.016 $\pm$ 0.009	0.027 $\pm$ 0.027	0.957 $\pm$ 0.010
SGDIFF	CVPR'25	0.980 $\pm$ 0.011	0.708 $\pm$ 0.119	0.668 $\pm$ 0.094	0.989 $\pm$ 0.005	0.020 $\pm$ 0.013	<u>0.024<math>\pm</math>0.022</u>	0.959 $\pm$ 0.011
<b>SALAD-PAN</b>		0.982 $\pm$ 0.010	<b>0.667<math>\pm</math>0.051</b>	<b>0.592<math>\pm</math>0.088</b>	0.991 $\pm$ 0.003	0.005 $\pm$ 0.002	<b>0.022<math>\pm</math>0.014</b>	<b>0.973<math>\pm</math>0.010</b>

**Qualitative comparison.** Figures 9 and 10 show representative visual comparisons on GF2 under RR and FR. We use the same band-to-RGB mapping and the same contrast stretching across methods, and green boxes mark the enlarged regions.

In Fig. 9, the first row shows the reconstructed results and the second row shows the corresponding error maps with respect to the ground truth. The zoomed region contains a small bright structure adjacent to darker surroundings, where inaccurate spectral mixing typically manifests as edge spreading and local color contamination. SALAD-Pan produces a cleaner transition in the zoom-in and its error map exhibits markedly weaker responses, indicating that fine structures are recovered with fewer residual distortions.

In Fig. 10, the PAN observation reveals clear geometric cues in the highlighted area, while the MS input remains blurred. SALAD-Pan reconstructs more coherent structures that better follow the PAN geometry, and the overall color appearance stays stable, which matches the improvement in  $D_s$  and HQNR in Table 8.

### F.2. WorldView-2 zero-shot transfer

We additionally present zero-shot transfer results on WorldView-2, abbreviated as WV2. The model is trained on other sensors and directly evaluated on WV2 with no retraining. This transfer setting is challenging because sensor-dependent spectral responses and PAN to MS coupling vary across platforms, and mismatched priors often lead to unstable colors or over-confident sharpening artifacts.

Figures 11 and 12 provide representative results under RR and FR. In Fig. 11, the zoom-in focuses on a compact high-contrast pattern that tends to collapse into a blurry blob when fine details are not properly recovered. SALAD-Pan restores a

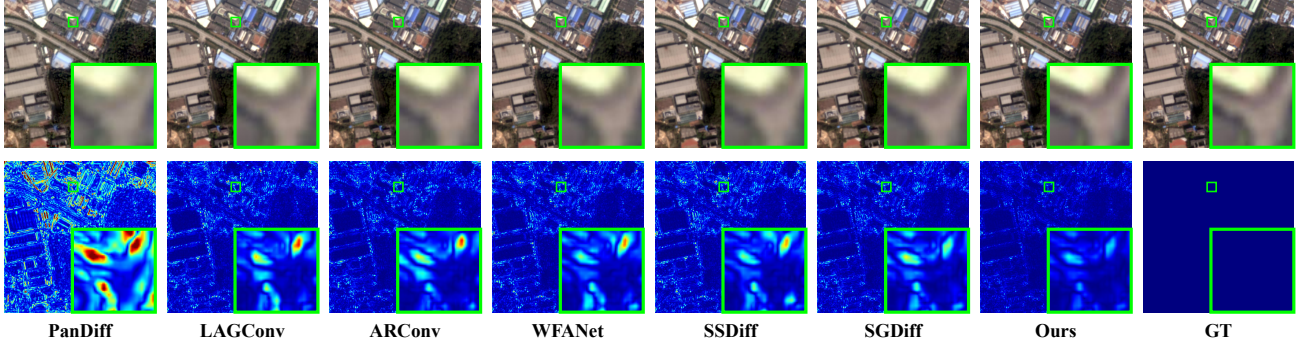


Figure 9. Visual comparison on GaoFen-2 (GF2) dataset at reduced resolution (RR).



Figure 10. Visual comparison on GaoFen-2 (GF2) dataset at full resolution (FR).

clearer localized configuration in the zoomed region and yields a noticeably weaker error response, suggesting improved reconstruction of fine structures under cross-sensor transfer.

In Fig. 12, some baselines exhibit visible chromatic artifacts near the bright structure in the zoom-in, with unnatural tints and smeared boundaries. SALAD-Pan follows the PAN-indicated geometry more faithfully while keeping the local tone consistent with the MS input, leading to more natural textures without exaggerated color shifts. Together, the WV2 visualizations support that the learned sensor-agnostic prior generalizes well to an unseen sensor domain.

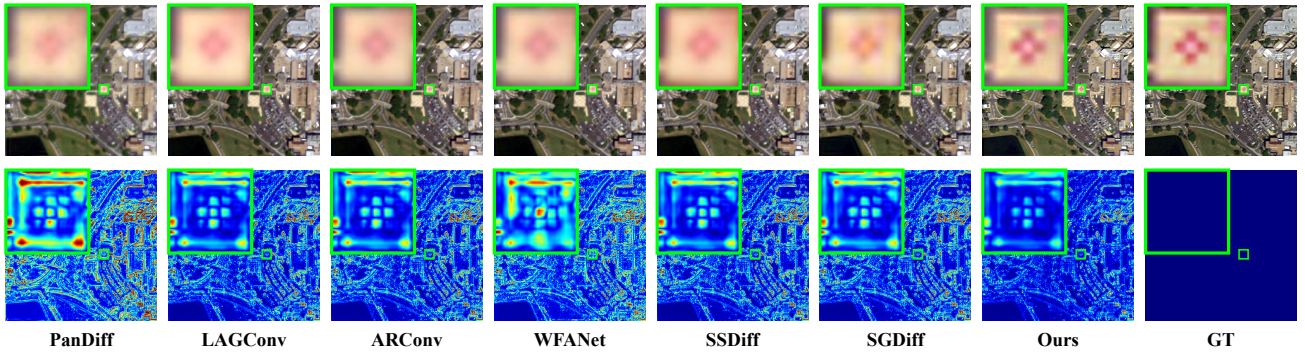


Figure 11. Visual comparison on WorldView-2 (WV2) dataset at reduced resolution (RR).



Figure 12. Visual comparison on WorldView-2 (WV2) dataset at full resolution (FR).